ABSTRACT

Non-Deterministic Modeling of the Bulk Thermal and Electrical Conductivity for Dense Thin Film Carbon Nanotube Networks

Nikhil A. Ashtekar, M.S.

Committee Chairperson: David A. Jack, Ph.D.

Thin films composed of single-walled carbon nanotubes, enjoy very high thermal and electrical conductivities, well beyond that of polymer matrix composites, and are very light in weight. Before these materials can experience industrial acceptance the underlying mechanisms dictating their performance must be understood. This research project intends to characterize using a physics based model the bulk thermal and electrical behavior of a neat carbon nanotube network conditions involving stochastic distributions of length, diameter, chirality, orientation obtained from the literature along with theoretical values of the inter-tube distance distribution obtained from in-house studies obtained through MD simulations. The work presents step by step development of the fully three dimensional model for linear, steady state loadings. Case studies using models are presented to better understand the dependence of the bulk thermal and electrical conductivity on the nanoscale parameters, such as bundle length, bundle diameter, orientation, volume fraction. The model is also used to investigate the sensitivity of the thermal and electrical conductivity on select stochastic parameters.

Non-Deterministic Modeling of the Bulk Thermal and Electrical Conductivity for Dense Thin Film Carbon Nanotube Networks

by

Nikhil A. Ashtekar, B.E.

A Thesis

Approved by the Department of Mechanical Engineering

William Jordan, Ph.D., Chairperson

Submitted to the Graduate Faculty of
Baylor University in Partial Fulfillment of the
Requirements for the Degree
of
Master of Science

Approved by the Thesis Committee

David A. Jack, Ph.D., Chairperson

Walter L. Bradley, Ph.D.

John M. Davis, Ph.D.

Accepted by the Graduate School
May 2011

J. Larry Lyon, Ph.D., Dean

Page bearing signatures is kept on file in the Graduate School.

TABLE OF CONTENTS

List of Figures vi

List of Tables ix

Acknowledgments x

Dedication xii

Chapter 1 Introduction 1

1.1 Road Map 4

Chapter 2 Carbon Nanotubes: A Brief Overview 6

2.1 History 6

2.2 Structure of Single Walled Carbon Nanotubes and Thin Films 7

2.3 State of the Art Information on Thermal Properties of CNTs 9

2.4 State of the Art Information on Electrical Properties of CNTs 14

Chapter 3 2D Thermal and Electrical Conductivity Models 19

3.1 Model Development 19

3.1.1 2 D Thickness Assumption 20

3.1.2 Periodicity 21

3.1.3 Development of Thermal 2D Model 23

3.1.3.1 Determination of Area of Overlap 25

3.1.4 Determination of Separation Distance Between the Tubes . . . 26

3.1.5 Determination of Thermal Conductivity 28

3.1.6 Thermal Model Implementation 29

3.1.7 Model Validation 32

3.2 Limitations of 2D Model 34

3.2.1 Modification of 2D Model 36

Chapter 4 3D Model 39
4.1 3D Model Development 39
4.2 3D Model Validation 44
Chapter 5 Case Studies 52
5.1 Representative Cell Dimensions 52
5.1.1 Representative Cell Dimension for 2D Model 53
5.1.2 Representative Cell Dimension For 3D Model 54
5.1.3 Representative Cell Construction Summary 56
5.2 Length Dependence of Conductivity 57
5.2.1 Thermal Conductivity Dependence on Bundle Length 58
5.2.2 Electrical Conductivity Dependence on Bundle Length 59
5.3 Diameter Dependence of Conductivity 61
5.3.1 Electrical Conductivity Dependence on Bundle Diameter . . . 62
5.3.2 Thermal Conductivity Dependence on Bundle Diameter 64
5.3.3 Comparison of Thermal Conductivity Dependence with the Electrical Conductivity Dependence on Bundle Diameter . . . 65
5.4 Conductivity Dependence on Volume Fraction 66
5.5 Conductivity Dependence on the Degree of Alignment of Tubes . . . 71
5.5.1 Electrical Conductivity Dependence on Orientation 72
5.5.2 Thermal Conductivity Dependence on Orientation 73
5.5.3 Difference in the Trends for Thermal and Electrical Conductivities with Increasing Orientation 74
Chapter 6 Sensitivity Analysis 75
6.1 Representative Element Dimensional Sensitivity Analysis 75
6.2 Parametric Sensitivity Analysis 80
6.2.1 Selection of Parameters 80
6.2.2 Determination of Sample Size 82
6.2.3 Determination of Appropriate Perturbation Size 82

6.2.4 Results 90

Chapter 7 Conclusions, Limitations and Recommendations 93

7.1 Conclusions 93

7.2 Limitations of the Model 95

7.3 Scope for Future Work 96

Vita 101

Bibliography 103

LIST OF FIGURES

1.1 Thermal transport between two carbon nanotubes. 1

1.2 Layer of thin film CNTs on an airplane made of composite material. . 2

1.3 Overview of the model. 4

2.1 Carbon nanotube network schematic. 8

3.1 Carbon nanotube network schematic. 20

3.2 Representative element tube configuration (a) Prior to periodic boundary conditions (b) After application of periodic boundary conditions. 22

3.3 Schematic depicting 2D nanoscale thermal flow, whereas the macroscopic flow remains 1D. 23

3.4 Area of overlap between two nanotubes. 26

3.5 Typical thermal element between two nanotubes. 31

3.6 Registry Response Surface. 32

3.7 CNT Thin Film Network. 32

3.8 Electrical conductivity as a function of cell thickness. 34

3.9 Histogram of contacts for the network from the table with $m = 10$, and $n = 100$. 37

3.10 Histogram of contacts from the equivalent 2D network and compared to the network from the table with $m = 0$, and $n = 100$. 38

4.1 Carbon nanotube network schematic. 41

4.2 Configuration of the CNT Network (a)Before periodicity and (b)After periodicity. 45

4.3 Representative element after application of periodic boundary conditions on (a)$+x_1$ edge, (b)$-x_1$ edge, (c)$+x_2$ edge, (d)$-x_2$ edge, (e)$+x_3$ edge and (f)$-x_3$ edge. 47

4.4 Final network after removal of tubes not participating in the network formation (a)Front view and (b)Top view. 48

4.5 Equivalent circuit representation of the CNT network. 49

5.1 Thermal conductivity κ in units of W/(mK) as a function of cell width ratio using 2D Model. 54

5.2 Relative error in thermal conductivity as a function of cell width ratio using 2D Model. 55

5.3 Thermal conductivity κ in units of W/(mK) as a function of cell width ratio using 3D Model. 56

5.4 Relative error in thermal conductivity as a function of cell width ratio using 3D Model. 57

5.5 Figure depicting the network formation with (a) Shorter naotubes, and (b) Longer nanotubes. 58

5.6 Thermal conductivity κ as a function of bundle length using 2D model. 60

5.7 Thermal conductivity κ as a function of bundle length using 3D model. 61

5.8 Electrical conductivity σ as a function of bundle length using 2D model. 62

5.9 Electrical conductivity σ as a function of bundle length using 3D model. 63

5.10 Plot depicting two system for same volume fraction, having (a) Thin cabonnanotubes, and (b) Thick carbonnanotubes. It is noteworthy, for a smaller diameter the number of alternative paths across the network are more. 64

5.11 Electrical Conductivity as a function of increasing diameter using 2D model. 65

5.12 Electrical Conductivity as a function of increasing diameter using 3D model. 66

5.13 Thermal conductivity κ as a function of bundle diameter for 2D model. 67

5.14 Thermal conductivity κ as a function of bundle diameter using 3D model. 67

5.15 Conductivity prediction as a function of bundle volume fraction for fixed length and diameter. 68

5.16 Conductivity prediction as a function of bundle volume fraction for length and diameter sampled from the Weibull distribution of Equation (3.24). 68

5.17 Electrical conductivity for select alignment states, as a function of orientation for 3D model. 73

5.18 Thermal conductivity for select alignment states as a function of orientation for 3D model. 73

5.19 Reduced options for networking for individual tubes with increasing alignment. 74

6.1 Response surface as a function of varying C_{W,h_2} and C_{W,h_3} predicted network conductivity for select cell width ratios in the x_1 direction, C_{W,h_1}. 77

6.2 Quiver plot of response surface slope vector for predicted network conductivity for select cell width ratios in the x_1 direction, C_{W,h_1}. 77

6.3 Response surface as a function of varying C_{W,h_1} and C_{W,h_3} predicted network conductivity for select cell width ratios in the x_2 direction, C_{W,h_2}. 78

6.4 Quiver plot of response surface slope vector for predicted network conductivity for select cell width ratios in the x_2 direction, C_{W,h_2}. 78

6.5 Response surface as a function of varying C_{W,h_1} and C_{W,h_2} predicted network conductivity for select cell width ratios in the x_3 direction, C_{W,h_3}. 79

6.6 Quiver plot of response surface slope vector for predicted network conductivity for select cell width ratios in the x_3 direction, C_{W,h_3}. 79

6.7 Decreasing error in approximating the population mean with increasing sample size. 84

6.8 Histograms showing the frequency distribution of electrical conductivity for increasing bundle length. 85

6.9 Histograms showing the frequency distribution of thermal conductivity for increasing bundle length. 87

6.10 Histograms showing the frequency distribution of electrical conductivity for increasing bundle diameter. 88

6.11 Histograms showing the frequency distribution of thermal conductivity for increasing bundle diameter. 89

LIST OF TABLES

5.1 Data used for various distributions. 72

6.1 Table of sample size and mean error. 83

6.2 Sensitivity results for electrical conductivity for increasing length. . . 84

6.3 Sensitivity results for thermal conductivity for increasing length. . . . 86

6.4 Sensitivity results for electrical conductivity for increasing diameter. . 89

6.5 Sensitivity results for thermal conductivity for increasing diameter. . 90

6.6 Relative sensitivity of the electrical conductivity to the weibull parameters. 91

6.7 Relative sensitivity of the thermal conductivity to the weibull parameters. 91

ACKNOWLEDGMENTS

I am indebted to a lot of people, who directly or indirectly contributed in accomplishing this work. I would like to express my gratitude to all those without whose support this work would not have been possible.

I would like to thank my advisor Dr. David A. Jack, for his support and encouragement in every phase of this project. I feel blessed with an advisor, who always finds time to listen to the problems and troubleshoot the technical glitches and setbacks that crop up from time to time. I highly appreciate his patience, in teaching me new concepts and improving my analytical skills. I am grateful to the members of my thesis committee Dr. Walter L. Bradley and Dr. John M. Davis for their constructive criticism and advice.

I would like to thank Dr. Les Lee and Dr. Jennifer Chase-Fielding of the Air Force Office of Scientific Research for supporting this endeavor and providing the resources for completing this project.

I am indebted to many of my colleagues who supported me. I would like to thank Agboola Babatunde and Cong Zhang for having fruitful discussions that helped me better comprehend some intricate concepts and helped me advance in my research. Special thanks to Theresa Vo, for granting me access to her computer system and letting my codes run.

My mother and father receive my deepest gratitude and love for supporting my decision of perusing graduate studies in the US and encouraging and motivating

me throughout. I am also grateful to my sister and my brother in law, for their love and support without which I wouldn't have made it this far.

It would have been really difficult for me to survive in this new environment away from my family without the help and support from my friends. I feel myself fortunate to have been blessed with wonderful people, who always tried to make me feel home. I am really honored to know all of them.

To aai and baba

CHAPTER ONE

Introduction

Carbon and Carbon allotropes have attracted a great deal of interest in recent years due to their unique structure and topology that creates a host of properties in these allotropes that are unparalleled by most known materials. Carbon nanotubes are one such allotrope that has caught the attention of researches for about two decades now. Studies have shown that these tiny quasi-one dimensional structures have promising properties that have the potential to revolutionize electronics, aviation and automobile industries. Figure 1.1 shows the thermal transfer between two carbon nanotubes. Chapters Three to Chapter Six explores the phenomenal properties of thin film networks composed of these single walled carbon nanotubes. These are being considered as the building material for the future.

One of the possible areas of application for which these allotropes has been investigated is the area of electrical and thermal management. Aircraft and satellites often encounter a situation when they have to make a compromise on thermal or electrical management on account of weight or vice versa. For instance, consider a case of a satellite revolving around a planet, during its course around the earth, it undergoes huge temperature fluctuations. When its position is behind the earth,

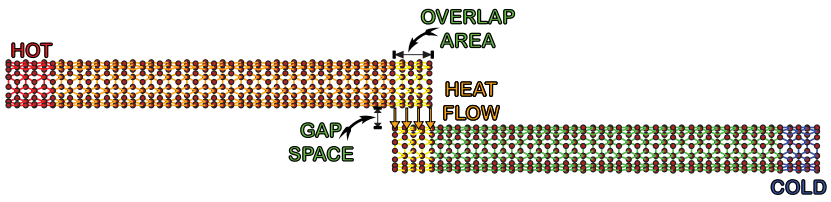

Figure 1.1: Thermal transport between two carbon nanotubes.

w.r.t sun, it is subjected to a very low temperature, as earth shields it from the hot infrared rays emitted from the sun. On the other hand, when it is directly facing the sun, the temperature raises considerably. This poses a thermal management issue, for the satellite design engineer. Consider another scenario, where the aviation industry is considering composite materials as an alternative over metallic components for building the structure of an aircraft, as described in Figure 1.2 due to their superior properties (high strength and low weight). A major concern with these composite structure is when the plane is struck by a lightning. The electric charge must be dissipated as soon as possible before it damages the plane. Carbon nanotube thin films (also referred to as a nanomembranes), are an excellent option for such a situations as they enjoy very high thermal and electrical conductivity, well beyond classical composite products and are very light in weight. Hence, researchers have proposed coating the surface of the plane with these thin films to protect the inner body of the plane. Lack of a systematic methodology to determine the nanostructures bulk

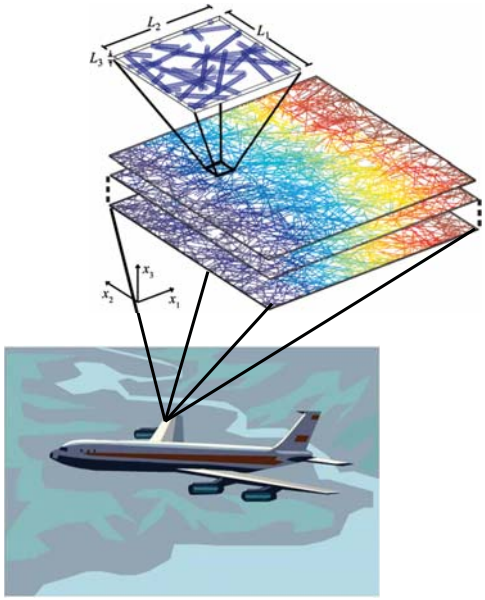

Figure 1.2: Layer of thin film CNTs on an airplane made of composite material.

thermal and electrical response makes employing carbon nanotube networks difficult for commercial applications, performance predictions and aircraft certification. Experimentation for various combinations of parameters is expensive, hence a guiding tool is needed to narrow down the experimental efforts. This research seeks to develop computational simulations to model the thermal and the electrical conductivity from a steady-state current loading of a macro-scale network of neat carbon nanotubes (CNT), and to capture, in a concise numerical model; the dependency bulk conductivity has on stochastic nanoscale effects.

Through this research endeavor a comprehensive physics based modeling effort for the thermal and the electrical characteristics of neat CNT thin films is presented using a 3D approach based off the finite element method. Knowledge of the dependence of bulk conductivity on individual nanostructured parameters will be beneficial for design, particularly considering the difficulty and expense of nanomembrane fabrication. Parameter variability as expected from inconsistencies caused by the manufacturing processes has been incorporated into the physics based model formulation, and includes; length, diameter, chirality ratios, and orientation of CNTs obtained from the literature, along with the inter-tube distance distribution obtained from in-house studies obtained through MD simulations.

The bulk conductivity of a nanotube network is a function of several phenomena of individual SWNT's such as length, diameter, chirality and deformations (vacancies and defects etc.) along with their interactions within the network, viz registry, tube contact angle, area of contact, length tubes in contact, and the orientation of tubes in a network etc. Figure 1.3 presents a brief overview of the inputs and the outputs of the model. Studies incorporating these phenomena are available in literature, but we have yet to find a single study incorporating all of them into a single full

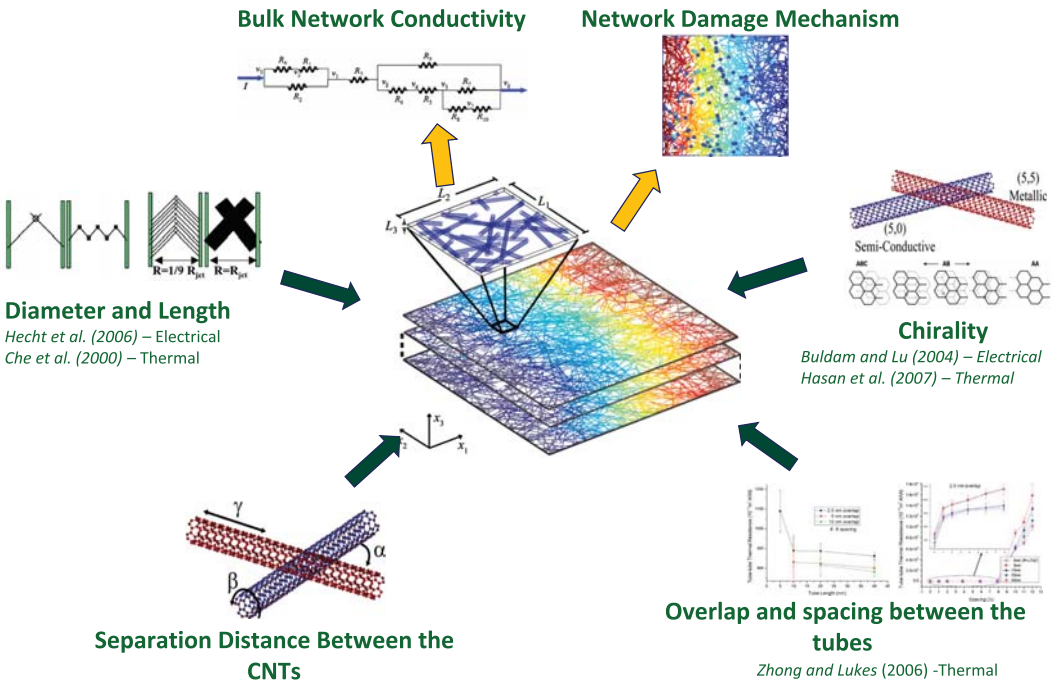

Figure 1.3: Overview of the model.

scale stochastic simulation based on the experimental simulation characterizations of the CNT network nanostructures and, in particular, for concentrations well above the percolation threshold.

1.1 Road Map

The motivation for this work comes from the need for a model to guide in manufacturing as well as the design of equipment with the thin film, and the inability of current models to accurately describe the conductivity behavior in different circumstances. The approach adopted to develop this model is documented in this thesis as discussed below.

The thesis begins in Chapter Two with a discussion on the history and the state of the art developments in the field of carbon nanotubes, with a focus on thermal and electrical conductivity. Chapter Three explains a step by step development of the 2 dimensional model and the assorted assumptions. The chapter also presents, in

detail, the physics involved along with the logic and math involved in programming the numerical model. Once the model is constructed we validated it with a two step approach, first for accurately implementing the logic and then against experimental results. The chapter concludes with the limitations of our 2D model and the need of the advanced, more realistic, three dimensional model. Chapter Four discusses the development of our 3D model, with the modifications on the boundary conditions and the validation procedures. The 3D model produces results that were very close to the real world experimental results. Chapter Five comprises of case studies conducted, once we were confident of the results generated by the model. The chapter begins with the determination of the appropriate dimensions for the representative element. This chapter also includes case studies on the length, the diameter and the orientation dependence on both the thermal and the electrical conductivities. The case studies presented will be beneficial to a design engineer or a manufacturing engineer dealing with high volume thin film carbon nanotubes. Chapter Six presents two sensitivity studies. The first one is the sensitivity of electrical conductivity to the dimensions of the representative element, and the second with the sensitivity of the thermal and the electrical conductivity to the variations in the weibull distribution parameters for diameter and length provided by Yeh [1] from her experimental SEM studies. Finally, in Chapter Seven we conclude with recommendations for further improvements on the model to improve the accuracy in the predicted results.

CHAPTER TWO

Carbon Nanotubes: A Brief Overview

Discovery of carbon nanotubes by Sumio Iijima [2] laid the foundations for the research of this novel material, which is predicted to be a material for the future. Since Iijima's discovery a lot of research has gone into investigating its outstanding structural, electrical and thermal properties. Even two decades since the discovery CNTs, they are still not used extensively on a commercial scale. The reason being the difficulty in the characterization on such a small scale, and predicting their behavior on a macro scale. Also, the unavailability of a cheaper manufacturing alternative discourages large scale production and application. This chapter presents a brief account on the history of carbon nanotubes and the current state of the art of these nano materials.

2.1 History

Sumio Iijima [2], in the year 1991, observed multi walled nanotubes formed in a carbon arc discharge. Since then, there has been extensive work in studying their unique self-bonding properties and the resulting structural, electrical, and thermal behavior. There have been considerable efforts to utilize their exceptional mechanical properties [3], structural properties [4, 5], electrical conductivity [1, 6–12] and their thermal conductivity [13–18]. Many researchers claim the carbon nanotube can be the building material of next generation engineering materials due to their exceptional behavior at the nanoscale. Unfortunately, to date, applications with nanotubes have been quite limited, due in large part to the inability to predict with any certainty the macroscopic response of industrial quality and scale products.

2.2 Structure of Single Walled Carbon Nanotubes and Thin Films

The SWNTs tend to form a bundle of parallel nanotubes [19], though isolated individual nanotubes [20] have also been reported. They are covered with soot on both the outer and inner surface. SWNTs are highly flexible, and can bend into a curved arc with a radii of curvature as small as 20nm. This flexibility indicates superior mechanical properties, and is consistent with the high tensile strength and bulk modulus of commercial and research grade vapor grown carbon fibers.

Studies have shown that the properties of SWNTs are strongly dependent on tubule diameter, making the diameter distribution of great interest to the researchers. Due to the difficulty in measuring physical measurements on SWNT, studies have been made on bundles of SWNTs. Early results on the diameter distribution of Fe-catalyzed single-wall nanotubes, indicates a range between $7\mathring{A}$ and $16\mathring{A}$, with $10.5\mathring{A}$ being the largest and $8.5\mathring{A}$ being the smallest peak in the distribution. For a co-catalyzed process, the peak in the distribution was found to be about $13\mathring{A}$.

A carbon nanotube (CNT) network depicted in Figure 3.7 is held together exclusively by van deer Waals forces between nanotubes. These networks are free-standing structures composed exclusively of CNTs aligned in a plane and have a unique combination of mechanical, electrical, and thermal properties as will be discussed in the next sections. Carbon nanotube networks have been fabricated within a magnetic field causing a preferred direction of alignment and studies have shown that these networks may have desirable conductive behaviors.

Hone and his group [21] produced, dense thin films of single wall carbon nanotubes and nanotube ropes using filtration/deposition from a CNT suspension in strong magnetic fields. They studied the electrical and thermal transport properties of these magnetically aligned single wall carbon nanotube films. They reported

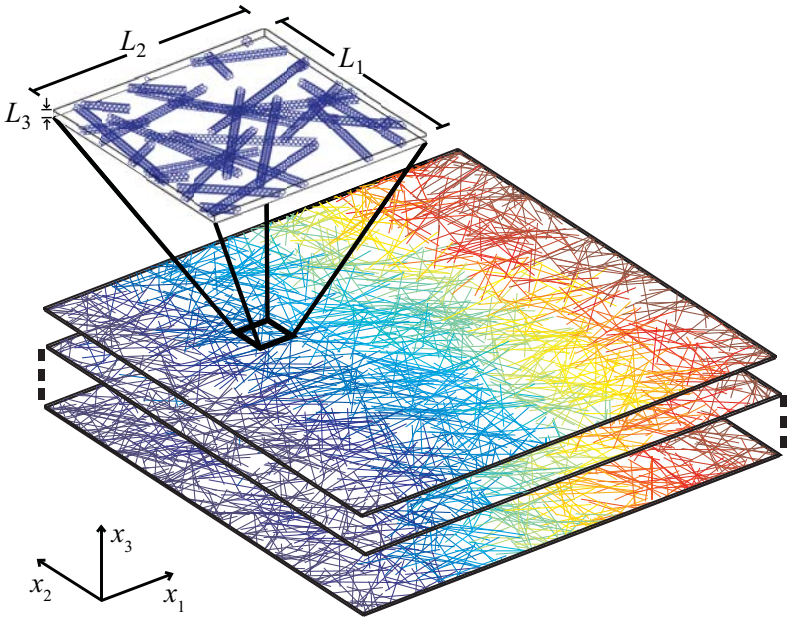

Figure 2.1: Carbon nanotube network schematic.

that the anisotropic morphology of magnetically aligned SWNTs leads to anisotropic electrical and thermal transport properties. Also, alignment results in increasing the parallel components of both the electrical and thermal conductivity w.r.t the unoriented material.

Gonnet [22] and his coworkers from Florida presented a technique to produce highly loaded and aligned single walled carbon nanotube nanocomposites by infiltrating SWNT mats with a low viscosity resin solution. They attained the in plane alignment by aligning the nanotubes in the buckypaper (high density CNT thin film) under a high magnetic field prior to the composite loading. They measured and reported the thermal conductivity for the buckypapers as well as their composites, and we will use their results to validate our thermal model. The conductivity trends and the value of conductivity was fairly in agreement with those of Gonnet's. The discrepancies what so ever was due to unavailability of complete data regarding the

length and diameter distribution etc, in their work. As will be shown in this work, knowing the length and diameter is essential for accurate predictions.

Ming Hu [23] and his fellow companions studied the phenomenon of thermal energy exchange between a carbon nanotube and the air. In their work the authors estimated that nanotube-air interfacial thermal conductance is about $0.1 MW/m^2K$,(which is equivalent to the resistance of a 250nm thick layer of air). Hu *et al.* conducted an MD simulation imposing a heat flux between the SWNT and air to study thermal interfacial conductance. The simulation was conducted on a $(10, 10)$ SWNT with diameter 1.34nm and 12.3nm long. The authors also concluded that the interfacial resistance strongly depends on the interaction parameters between air atoms (which in this case were Oxygen 22% and Nitrogen atoms 78%) and the carbon nanotube. Therefore, in their opinion, a further study of the interactions between the nanotube and the oxygen and nitrogen molecules is required in order to predict the interfacial thermal resistance accurately. Currently all of our models (Thermal 2D and 3D, Electrical 2D and 3D) consider a neat thinfilm carbon nanotube network, i.e. a network without any matrix surrounding it. In other words, the network is surrounded by air. Hence, we used the results from this work to calculate and compare the resistance for our thermal model, i.e. resistance between a nanotube and air, with its intrinsic resistance and intercontact resistance.

2.3 State of the Art Information on Thermal Properties of CNTs

J.Che *et al.* [24] studied the thermal conductivity of carbon nanotube and its dependence on defects and vacancies, using equilibrium MD simulations. They derived the Green Kubo relation from linear response theory which was then used to extract the thermal conductivity from heat current correlation. They found that once the system is large enough the theoretical value of thermal conductivity converges

to a constant. For a defect free $(10, 10)$ SWNT, they reported the theoretical value to be 29.8W/mK along the tube axis. From their study, they also found that the thermal conductivity decreases as the vacancy concentration increases. The same effect was observed with conformational defect. Chico *et al.* [7] studied the effect of pentagon-heptagon defects into the hexagon network of SWNT. They used the tight binding method and calculated the electronic structure of such systems. They reported that such systems behave as a nanoscale metal/semiconductor or semiconductor/semiconductor junctions.

Yang *et al.* [18] studied the thermal conductivity of multiwalled carbon nanotubes, prepared by using a microwave plasma chemical vapor deposition. The group employed the pulsed photothermal reflectance technique, and found that the average thermal conductivity of carbon nanotube thinfilms, with thickness $10 - 50\mu$m is around 15 W/m-K at room temperature independent of the tube length. From their study they also suggested that the heat transport in the MWNT's is dominated by phonons. Our model currently assumes all the tubes to be single walled. Multiwalled nanotubes being cheaper, can be studied and incorporated in the model.

Zhang *et al.* [25] studied the chirality dependence of the thermal conductivity of carbon nanotubes. The group studied three types of SWCNTs (armchair, chiral and zigzag) using the homogeneous non-equilibrium Green-Kubo method based on the Brenner potential. From their simulations they concluded that the thermal conductivities of all three types of nanotube had similar temperature dependence, and the chiral nanotube had the lowest thermal conductivity.

K. Bi *et al.* [26] studied the thermal conductivity of SWNTs using both the equilibrium molecular dynamic (EMD) and non-equilibrium molecular dynamic (NEMD) techniques. From their study of length dependence on thermal conductivity

of CNT using both the techniques they found that, the results obtained from EMD technique is reasonably larger than that from the other. They reported the range of thermal conductivity for SWNT's ranged from 400W/mK to 600W/mK. This was far less from the one reported by Che *et al.* [24], which was 2980 W/mK. Bi *et al.* attributed this ambiguity to the difference in the way the cross sectional area was defined in both the papers and also to the fact that their work neglects nonbond order interaction, whereas Che considered the non bond order interaction in the Brenner-type potential. The group also found that the thermal conductivity increased with increasing tube length as opposed to the convergence reported by Che. According to them this may be attributed to the difference in the integaration methods of the HCACF adopted by the two groups. Bi *et al.* [26] also investigated the temperature dependence of three different type of CNTs, one perfect tube and two tubes with defects containing isotropic atoms and vacancies. For all the three tubes they found that the thermal conductivity dropped as the temperature increased. Also, with increase in temperature, the difference in the conductivity of the vacancy adulterated tube and the other two tubes became less.

Hone and his group [27] at University of California at Berkley, also studied the temperature dependence of crystalline ropes of single walled carbon nanotubes for temperatures ranging from 8K to 350K. They found that the thermal conductivity decreases linearly with decreasing temperature; also it displays linear temperature dependence below 30K. They also concluded that the thermal conductivity is dominated by the phonons at all the temperatures. Osman and Srivastava [17] in their study on temperature dependence of the thermal conductivity of single-wall carbon nanotubes concluded that for all the cases the thermal conductivities show a peaking behavior before falling off at higher temperatures. They also reported that the peak position

shifts to higher temperatures for nanotubes with larger diameters. In their molecular dynamics simulations with the Tersoff-Brenner potential for C-C interactions, over a temperature range of $100 - 500$K, they found no significant chirality dependence on thermal conductivity. Philip Kim and his group [28] studied the mesoscopic thermal transport and energy dissipation in carbon nanotubes. In their experiment they used a microfabricated suspended device to measure the thermal conductivity of an individual multiwalled carbon nanotube. They found that at room temperatures the observed thermal conductivity is more than 3000 W/m-K.

Motoo Fujii [29] and his group from Japan, experimentally measured the thermal conductivity of a single carbon nanotube using a suspended sample attached T-type nanosensor. They found that the thermal conductivity of a carbon nanotube increases as the diameter decreases. For a nanotube of diameter 9.8nm, they found the thermal conductivity to exceed 2000 W/mK. They also conducted a study on the temperature dependence of the carbon nanotubes with a diameter of 16.1nm and found that it has an asymptote near 320K. In our model we deal with the bulk conductivity of thin films in general. We conducted a case study on diameter dependence and found that the bulk thermal conductivity as well as the bulk electrical conductivity decreased with an increase in tube diameter.

Zhong and Lukes [16] studied the interfacial thermal transport between offset parallel $(10, 10)$ single-wall carbon nanotubes using molecular dynamic simulations and analytical thermal modeling as a function of nanotube spacing, overlap, and length. From their studies they reported that the thermal resistance decreases with an increasing area of overlap. They also presented their results in the form of a plot for increasing thermal resistance with increasing spacing between the tubes. Our

thermal models currently uses the values from their plot to determine the intercontact thermal resistance, as a function of the separation distance between the tubes.

Satish Kumar *et al.* [13] from Purdue, developed a computational thermal model for nanotube based electronic display. The group predicted the temperature rise in the tube network and substrate, along with the effect of tube-tube contact conductance, tube-substrate contact conductance and substrate-tube conductivity ratio on the temperature rise. They studied the effect of convective cooling on the temperature rise for a range of heat transfer coefficients between the display surface and the ambient air. From their study they reported that the tube-substrate contact resistance is a dominant resistive component for the tube temperature rise, but was found to be insignificant for the substrate temperature rise. The group also concluded that the tube conductivity and tube-tube contact conductance are found to have only a minor effect on lateral heat spreading as the dominant resistance to heat removal lies on the substrate and the air side for the range of parameters investigated.

Sayed Hasan *et al.* [14] studied the effect of hot phonon scattering on CNT FET. From their hot-phonon simulation of CNT MOSFET they reported that for a single tube, heating does not seem to be a problem. They also reported that, at high gate bias, the hot-phonon effect can reduce the ballistic current by 33% and the unit gain cutoff frequency by 56%.

Shiren Wang *et al.* [30], studied the dispersion and the thermal conductivity of carbon nanotube composites. In this work they proposed an effective way to improve dispersion of CNTs into polymer matrices that also retained the perfect electronic structure of CNTs. The group was able to shorten single walled nanotubes and use this in polymer composites. Using AFM and SEM techniques, they were able to conclude that shortening of the nanotubes significantly improved the CNT dispersion

awhich in turn effectively improved the percolation. Also, the thermal conductivity of composites containing short CNTs were found to be much better than those containing pristine CNTs.

Salvin *et al.* [31] numerically studied the thermal conductivity of single walled carbon nanotubes for two cases. First for an isolated carbon nanotube and second for a nanotube interacting with a substrate. In their study they found that irrespective of the potential and the numerical method employed the character of the thermal conductivity depends crucially on the interaction between a nanotube and a substrate, whereas an isolated infinite ideal single-walled carbon nanotube which is not fixed on a substrate demonstrates anomalous thermal conductivity. From their studies on the dependence of the thermal conductivity coefficient on temperature, they found that the carbon nanotube demonstrates similar anomalous thermal conductivity for all temperatures in the range $T \leq 500$ K.

2.4 State of the Art Information on Electrical Properties of CNTs

J. Tersoff [32] while studying the contact resistance of carbon nanotubes pinpointed two basic reasons for high contact resistance of CNT and also has given suggestions to reduce it.

Hecht *et al.* [33] studied the dc conductivity dependence of single walled carbon nanotubes networks on average bundle length and diameter. They found that σ_{dc} varied as $\sigma_{dc} \sim L_{av}^{1.46}$ for the bundles with a fixed diameter, $L_{av}^{1.46}$ is the average bundle length. From their study they also reported that the exponent of L, would be between 0 and 2.48, with the former being a network dominated by ballistic resistance (which is assumed zero in our simulations) and the later value for an isotropic network dominated by intercontact resistance. The exponent of $1.9 \sim 2$ in our study is within the range proposed by Hecht *et al.*'s results, but is not equal to the upper limit as

expected for a network dominated by inter-contact resistance. The discrepancy is attributed to the differences in how we handle multiple contacts for a given tube. They assume perfectly rigid bundles with each tube having a single point of contact, whereas in our situation with the nanotubes filling 60% of the volume for the 3.0μm long tubes, each individual nanotube will average 80 contact points, and there will exist a significant percentage of tubes with over 100 points of contact. Similarly for diameter dependence they noted that the exponent would be ~ -2 for perfectly rigid bundles. But from the case study we conducted using our model we found the exponent to be -2.94 to -3. This discrepancy is again attributed to the fact that Hecht *et al.* assumed that each tube would have a single point of contact, whereas in our situation with the 5nm diameter nanotubes an individual nanotube will average just less than 80 contact points.

Reto Haggenmueller *et al.* [34], in their study of thermal and electrical conductivity of single wall carbon nanotube/polyethylene nanocomposites, studied the thermal and electrical conductivities of the nanocomposite in terms of SWNT loading, the degree of polyethylene (PE) crystallinity, and the PE alignment. They found out SWNT/PE composites made with high density PE (78% crystalline) exhibit higher thermal conductivity than composites made with low density PE (33% crystalline). From this result they concluded that the higher crystalline matrix reduces the interfacial thermal resistance by providing more crystalline- PE bridges between nanotubes. The experiments also showed that melt fiber spinning of SWNT/HDPE nanocomposites with low loadings produces composites in highly aligned SWNT and oriented polyethylene crystallites. The thermal conductivity along the alignment direction increases with PE alignment regardless of the SWNT loading, while the electrical conductivity along the fiber decreases. Finally the authors concluded that the SWNT

filler dominates the electrical conductivity of the SWNT/polymer composites, while the thermal conductivity depends on both the SWNT filler and the semicrystalline PE matrix.

Giang Pham *et al.* [35] studied the mechanical and electrical properties of polycarbonate nanotube thin film ("buckypapers") composite sheets, that were produced by infiltrating SWNT films with a polycarbonate solution. The group observed that the stiffness and toughness of these sheets increased with the addition of polycarbonate, but the electrical conductivity decreased. Also, polycarbonate/buckypaper composite sheets showed higher resistance to handling and processing damages. The group also presented a bulk resistance value of 0.0049 Ω/cm for a buckypaper.

Park *et al.* [36] studied the high current-carrying capacity of various carbon nanotube-based thin films. They exposed the buckypapers to high electrical current densities under different environments. From their study they concluded that SWCNT thin films breakdown near 430^oC in ambient conditions, with a flash of light. Also, mixed composite films of SWCNTs and MWCNTs showed higher ignition temperatures of over 500^oC.

Wang et al. studied the processing and property of the single-walled carbon nanotube (SWNT) thin film/epoxy resin matrix nanocomposites. With the technique developed in their work, the storage moduli is demonstrated to be as high as 15 GPa. The research results also indicated that the proposed infiltration technique was capable of fabricating nanocomposites with a controllable nanostructure and high SWNT loading.

Tian *et al.* [37] studied the fabrication of single-walled carbon nanotube/polyelectrolyte multilayer composites by layer-by-layer assembly and magnetic field assisted alignment. In their study they combined the layer-by layer assembly

technique with magnectic force-induced alignment to fabricate SWNT/PEI multilayer composites. From their study the group concluded that the LBL/magnetic alignment approach has the potential for fabricating nanotube composites with highly ordered nanostructures for multifunctional materials and device applications.

Qunfeng Cheng *et al.* [38], studied multi-walled carbon nanotube sheet/bismaleimide nanocomposites. In their study they achieved tensile strength of over 2 GPa, with a Young's modulus of 169 GPa. They reported the electrical conductivity of this nanocomposites to be 5500 S/cm along the alignment direction. The reason for these better mechanical properties were attributed to the coupling effects of millimeter-long MWNTs, mechanical stretching, and prepregging under high pressures, which led to higher loading, better alignment and enhanced load transfer. Also, better dispersion of the nanotube ropes into spread-out extra-thin films led to better contacts among MWNTs, giving rise to the effective load transfer and enhanced electrical conductivity.

Jin Gyu Park *et al.* [39] studied the electromagnetic interference shielding properties of carbon nanotube buckypaper composites. For their study they used different nanocomposite laminates consisting of various proportions of single-walled and multi-walled carbon nanotubes, having different conductivities, and with different stacking structures. From their study, they concluded that, the shielding effectiveness of the CNT thinfilm composites mainly depended on the conductivity and thickness of the layers. Further, SWCNTs or long-MWCNT thin films, provide better EMI shielding due to their high electrical conductivity. But, they also found that increasing the number of layers by adding on to the composite surface showed some limitations toward realizing high EMI shielding performance due to a lack of multiple reflections. Jin Gyu Park [40] also produced carbon/carbon composites consisting of single-walled

carbon nanotube (SWCNT) thinfilm and mesophase pitch resin through impregnation of BP with pitch using toluene as a solvent. In their study they filled in the voids in the carbon/carbon composite sample, by repeating a cycle of drying, stabilization and carbonization processes. They found that the electrical conductivity and the density of the composites increased with carbonization, by 2 to 3 times. The electrical conductivity rose from 200 S/cm to more than 400 S/cm at room temperature. From their study they concluded that the discontinuity and intertube contact barriers of SWCNTs may be partially overcome by the carbonization process of pitch.

CHAPTER THREE

2D Thermal and Electrical Conductivity Models

This chapter presents the initial approach adapted to determine the bulk thermal and electrical behavior of thin films employing 2 dimensional models with emphasis on the thermal model. The chapter begins with the discussion on CNT thin films and basic assumptions made by us for our models. Especially noteworthy is the volume assumption, which loosely states that, the thickness of a representative element can not influence the bulk conductivity. A case study is conducted to demonstrate the flaw in this assumption as was presented in [41].

3.1 Model Development

The model uses the stochastic parameters, bundle length l_i, bundle diameter d_i, chirality of the tubes and the orientation. The model restricts the orientation and placement of the tubes to a single plane (x_1-x_2 plane), and allows the center of mass of the tubes to move within the plane. The tubes are assumed to be longitudinally rigid, with a small local deformation occurring in the transverse direction, due to the van der Waals forces between the tubes. A unit cell is selected, as shown in Figure 3.1, of dimensions L_1, L_2 and L_3, along respectively the x_1, x_2 and x_3 directions. Values of θ_i (planar orientation angle), l_i (bundle length), d_i (bundle diameter), c_i (bundle chirality), $\mathbf{x_i}$ (bundle spatial position, where $\mathbf{x_i} \in \mathbb{R}^2$) are selected for a set of bundles with $i \in (1, 2, ..., N_t)$. The number of tubes N_t within the cell is selected to satisfy the desired volume fraction of CNTs, V_{CNT} through the following relationship:

$$V_{CNT} = \frac{\pi}{4} \frac{\sum_{i=1}^{N_f} l_i d_i^2}{L_1 L_2 L_3} \tag{3.1}$$

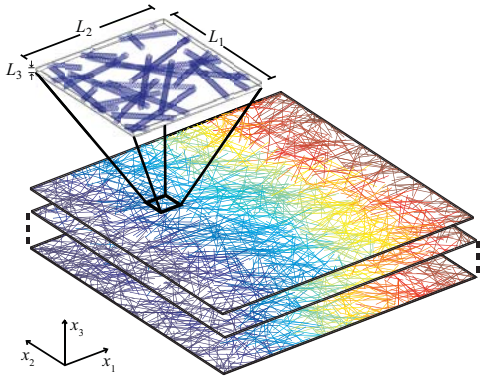

Figure 3.1: Carbon nanotube network schematic.

Notice, if the tubes are not all of identical lengths and diameters, one cannot, in general, replace the relationship in Equation (3.1) with:

$$V_{CNT} = \frac{\pi N_f \mu_l \mu_d^2}{L_1 L_2 L_3} \tag{3.2}$$

where μ_l is the mean value of the length distribution and μ_d is the mean value of the diameter distribution. For instance, consider 5 CNTs of lengths 2μm, 2.5μm, 2.8μm, 2.6μm and 2.5μm and diameters 20nm, 25nm, 19nm, 22nm and 26nm respectively, in a cell of dimensions 1×10^{-5}, 1×10^{-5} and 1×10^{-7}. Equation 5.6 would provide 4.8×10^{-4} as the volume fraction whereas the volume fraction predicted by Equation 3.1 is 4.96×10^{-4}.

3.1.1 2 D Thickness Assumption

It is necessary to quantify appropriate cell thickness L_3 or cell height even for evaluating the $2D$ planar network. Yeh [1] selected the cell height to correspond to the maximum nanotube diameter sampled from the weibull distribution, and a similar assumption was made in [8]. This was (see e.g. [1,8]), made with the assumption that the choice of the cell width should have no bearing on the resulting conductivity of

the network. The approach adopted to reduce the 3D model to 2D was incorrect as shown in [41].

3.1.2 Periodicity

At the macroscopic level a thin film contains many nanotubes to form the network. It is computationally infeasible to consider each tube forming the network for computation of thermal or electrical conductivity. Hence, we desire a representative area of appropriate dimensions that will be small enough to be calculated on a work station, while reasonably representing the bulk conductivities of the macroscopic network. The representative element must satisfy the following two considerations:

1. The representative element must be periodic, i.e., adjacent elements must be continuous, thus imposing a geometric continuity of adjacent sides within the element.

2. The element must be large enough to capture the stochastic nature of all chiral, spatial and geometric effects, but it is desired it will be small enough to be calculated on a work station.

To ensure continuity, the model constrains a tube exiting one edge to enter the converse element edge. Figure 3.2 is presented to visualize these boundary conditions. Observe the red tube in Figure 3.2(a), prior to the application of periodicity, sticking out of the $-x_2$ face, and after the application of the periodic boundary conditions, seen in Figure 3.2(b), the portion of the tube sticking out of the $-x_2$ face reenters from the $+x_2$ face. The same holds true for the remaining tubes sticking out of the representative element.

Along with geometric periodicity, flow continuity must also be considered. Figure 3.3 it is desired that the macroscopic bulk flow is constrained from $-x_1$ to

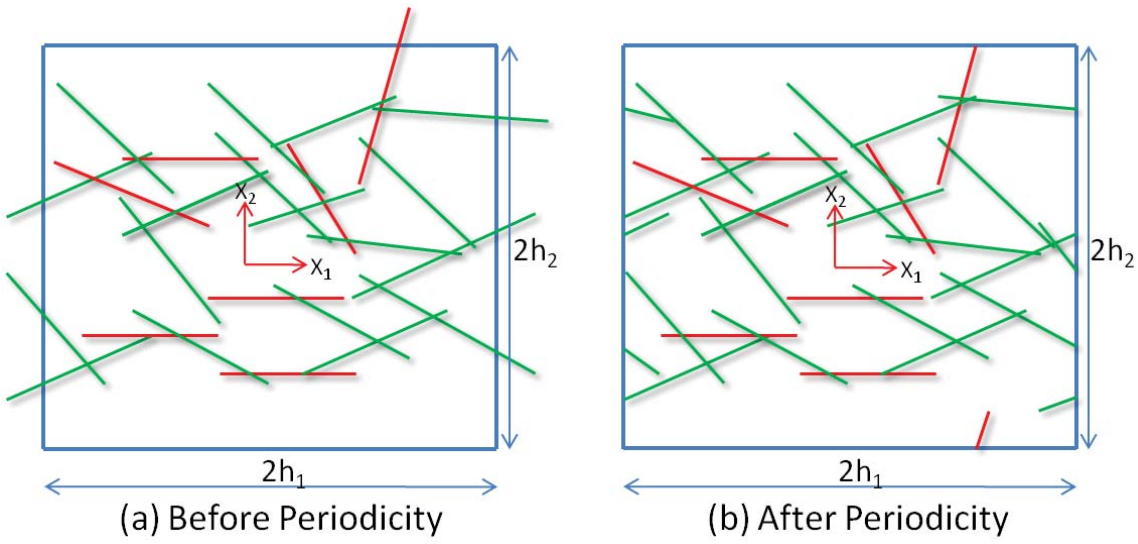

Figure 3.2: Representative element tube configuration (a) Prior to periodic boundary conditions (b) After application of periodic boundary conditions.

x_1, but on the nanoscale the thermal current can flow along the tubes. Hence, the current path is effectively $2D$. To ensure that the representative element satisfies the desired macroscopic flow behavior, the bulk thermal current passing through the $x_2 = \pm L_2/2$ edge is mapped through the $x_2 = \mp L_2/2$ edge with no energy loss. The tubes passing through the $x_1 = L_1/2$ face are all of the same temperature T_+ and the tubes passing through the $x_1 = -L_1/2$ face are all of the same temperature T_-.

To determine the bulk conductivity, a small representative element is selected from the i^{th} layer, $i \in \{1, 2, ..., N_L\}$, where N_L is the total number of layers. The sample selected is sufficiently large enough such that all geometric effects of consideration are periodic in nature on all opposing surfaces and all local effects are small in comparison to the elemental size. To ensure this, a case study is presented in the results section to determine the appropriate cell size. The sampling process of each variable is performed using a Mote-Carlo sampling technique of N_f samples (see e.g., [42] for a discussion of the M-C technique), where N_f is chosen as the smallest

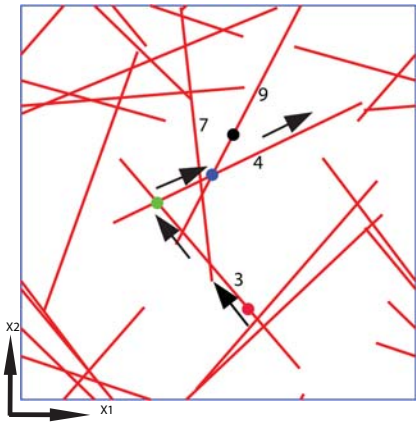

Figure 3.3: Schematic depicting 2D nanoscale thermal flow, whereas the macroscopic flow remains 1D.

integer number to satisfy

$$V_{CNT} \leq \frac{\pi}{4V_{RE}} \sum_{i=1}^{N_f} d_i^2 l_i \tag{3.3}$$

where V_{RE} is the volume of the representative element and V_{CNT} is the desired volume fraction of CNTs using the classical definition of volume fraction of a composite inclusion where in this case the matrix is air.

3.1.3 Development of Thermal 2D Model

The model is based on the idea that the overall thermal resistivity of a thin film network, can be divided into the following three components:

1. Thermal resistivity along a nanotube [24].

2. Thermal resistivity between individual nanotubes [16].

3. Thermal resistivity between the thin film network and surrounding media, where in the present context the media is air [23].

The model assumes the dominating factor within the network is the intercontact resistance, and thus the intrinsic resistance is neglected. This assumption is based off the fact that a typical intercontact resistance value is in the range $2 \times 10^{-5} - 1.6 \times 10^{-4}$m^2-K/W (see e.g. Lukes and Zhong [16]). For a tube of say, diameter 16.1nm as studied by Fuijii [29] using the relation:

$$A_e = \frac{D_1 \times D_2}{sin\gamma} \tag{3.4}$$

Where D_1 and D_2 are the diameters of the overlapping tubes and γ is the angle between them, the area of overlap is about $2.6 \times 10^{-16} m^2$, thus the thermal resistance is in the range $7.72 \times 10^{10} - 6.17 \times 10^{11}$ K/W. Now, the intrinsic resistance for the same nanotube of diameter 16.1nm as described by Fuijii [29] at 320K, having aspect ratio of say 200 can be computed using the relation $l_e/(A_e \times k_e) \approx 9.89 \times 10^6$ K/W. Comparing the magnitudes of thermal conductance, it seems reasonable to neglect the intrinsic conductance of the tube. Thus for the present model we assume that the thermal resistance along the nanotubes is negligible relative to the resistance at the junction. The thin film is neat, i.e., has no matrix, thus all tubes are surrounded by air, which acts as an insulator [43, 44]. In other words, we will assume there is negligible amount of thermal current flow from the network to the surroundings. We also assume for the present study that Fourier's law for heat transfer in the linear regime is valid for small thermal loadings. Also, there is continuity of heat flow without any system leakage, and discontinuity occurs only at the points of contact between the tubes. In other words, if s is the direction of flow of thermal current along the tube, then:

$$\frac{dQ}{ds} = 0 \tag{3.5}$$

where Q represents the heat flow. Hence, the thermal potential function ψ between the tubes is the only consideration and is governed by the constitutive equation:

$$\frac{\partial^2 \psi}{\partial \hat{x}^2} = \alpha_{ij} \left(\tilde{T}_i - \tilde{T}_j \right) \tag{3.6}$$

where $\hat{x}^2$ is a point in space between the i^{th} and j^{th} tubes, respectively, and α_{ij} is expressed in terms of the effective thermal conductivity between the tubes. Using a finite element approach with 1D elements between nanotubes, as depicted in Figure 3.5 for the overlapping regions in yellow, Equation (3.6) can be recast as (see e.g. Reddy [45] for a complete description)

$$\frac{A_e k_e}{h_e} \begin{bmatrix} 1 & -1 \\ -1 & 1 \end{bmatrix} \begin{Bmatrix} T_1^e \\ T_2^e \end{Bmatrix} = \begin{Bmatrix} Q_1^e \\ Q_2^e \end{Bmatrix} \tag{3.7}$$

where the term $\frac{A_e k_e}{h_e}$ represents the thermal conductance, A_e is the cross sectional area of contact, h_e is the separation distance, k_e is the thermal conductivity of the element, T_i^e is the temperature of the i^{th} tube and Q_i^e is the heat flow passing either out of the 1^{st} tube or into the 2^{nd} tube, which will be the same in this case.

3.1.3.1 Determination of Area of Overlap

In order to determine the area of overlap A_e) between the tubes consider Figure 3.4, which depicts two overlapping tubes with diameters D_1 and D_2 at an angle γ. In ΔABM

$$AB = \frac{D_1}{\sin \gamma} \tag{3.8}$$

Similarly, in ΔADN

$$AD = \frac{D_2}{\sin \gamma} \tag{3.9}$$

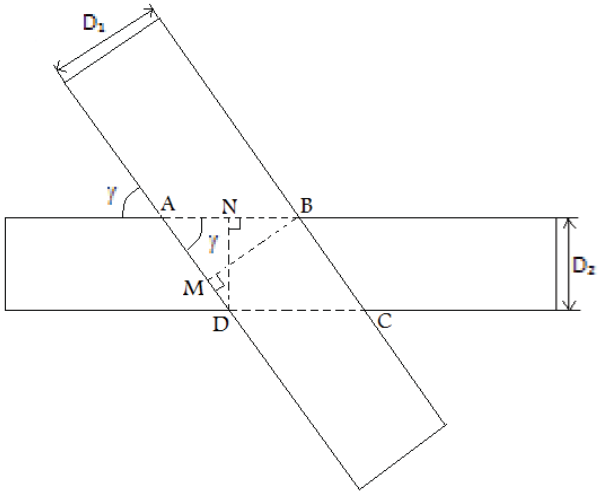

Figure 3.4: Area of overlap between two nanotubes.

Now, The area of parallelogram $ABCD$ can be determined as:

$$\square ABCD = AB \times AD$$

$$\square ABCD = \frac{D_1 D_2}{\sin^2 \gamma} \sin \gamma$$

$$\square ABCD = \frac{D_1 D_2}{\sin \gamma}$$

The above relation holds true for large value of γ. If $\gamma \approx 0$ then, the area of overlap is given by:

$$\square ABCD = min(D_1, D_2) \times L \tag{3.10}$$

where, L is the length of ovaerlap.

3.1.4 Determination of Separation Distance Between the Tubes

Nanotubes can be broadly classified either as metallic or semiconducting. It has been shown by [44] that the electrical conductivity of the network alters considerably with the change in the ratio of metallic to semiconducting tubes in the

network. Though the direct impact of this ratio on bulk thermal conductivity is still unclear, chirality is considered only through the separation distance function of Equation (3.12). We assume the metallic tubes to compose $1/3^{rd}$ of the overall population and the remaining $2/3^{rds}$ of the tubes are semiconducting [46]. Thermal resistance between the tubes depend on the separation distance as can be noted from Equation (3.7). For the study of separation distance between the tubes, we considered a $(5,0)$ to represent the metallic tube and a $(5,5)$ tube to represent a semiconducting tube. This separation distance was studied, using molecular dynamic simulations as a function of angle between the intersecting tubes (δ), rotation of one tube about its own axis (ξ) and position (sliding) effect (ϖ) as shown in Figure 3.6. In order to study these effects, two CNTs were held perpendicular to each other in the same plane. One of the tubes was fixed at both the ends and the angle between the tubes (δ) was varied by rotating the opposing tube, with a step size of 5^o. The results obtained were tabulated for angles between 0^o to 90^o. Similar runs were made by rotating one CNT about its own axis (β). Additional simulations were made by sliding one tube along the second and rotating it about the longitudinal axis (γ). Based on all of our simulations, it was observed that the results were reasonably fit by a normal distribution with mean and variance expressed as,

$$N(x,\mu,\sigma) = \frac{1}{\sigma\sqrt{(2\pi)}} e^{-(x-\mu)^2/(2\sigma^2)} \tag{3.11}$$

The distributions employed in the present study for h_e are given as:

$$\begin{aligned} h_e &= \mu_{MM} + \sigma^2 x - d(5,0) \\ h_e &= \mu_{MS} + \sigma^2 x - \frac{d(5,0) + d(5,5)}{2} \\ h_e &= \mu_{SS} + \sigma^2 x - d(5,5) \end{aligned} \tag{3.12}$$

here, μ_{MM}, μ_{MS} and μ_{SS} are respectively, the mean separation distances between the metallic-metallic, metallic-semiconducting and semiconducting-semiconducting nanotubes and $d(5,0)$ and $d(5,5)$ are there respective diameters of the metallic $((5,0))$ and the semiconducting $((5,5))$ tubes. The separation distance obtained from the MD simulations was measured between the centroids of the tubes, hence the diameters are subtracted in order to get the separation distance between the surfaces. The values for μ_{MM}, μ_{MS} and μ_{SS} is obtained from the following distribution:

$$\text{where, } \begin{cases} \mu_{MM} = 9.3 \times 10^{-10}, & \sigma^2_{MM} = 0.27 \times 10^{-10} \times U - 6.78 \times 10^{-10} \\ \mu_{MS} = 7.9 \times 10^{-10}, & \sigma^2_{MS} = 0.1 \times 10^{-10} \times U - 5.345 \times 10^{-10} \\ \mu_{SS} = 6.4 \times 10^{-10}, & \sigma^2_{SS} = 0.17 \times 10^{-10} \times U - 3.91 \times 10^{-10} \end{cases} \tag{3.13}$$

$$U(x) = \frac{1}{\sigma\sqrt{2\pi}} e^{-(x-\mu)^2/\left(2\sigma^2\right)} \tag{3.14}$$

These distributions were obtained by MD simulations on a pair of metallic(M), and a semiconducting(S) tubes for a function of angle between the intersecting tubes (δ), rotation of one tube about its own axis (ξ) and the relative position of one tube over the other (sliding effect) (ϖ) as shown in Figure 3.6 and discussed in the preceding section.

3.1.5 Determination of Thermal Conductivity

Zhong and Lukes [16] studied the thermal resistance between overlapping $(10,10)$ tubes using molecular dynamic simulations and provided graphical results for the inter-contact thermal resistance as a functions of both, cross-sectional area and the separation distance. A rudimentary curve fit was made to their data, and the resulting linear fit to their results for thermal conductivity between tubes is:

$$K_e = -5 \times 10^{-15} h_e + 1 \times 10^7 \left(\frac{\mathrm{W}}{\mathrm{m^2K}}\right) \tag{3.15}$$

where h_e is the separation distance given in units of meters. As the study was for only one single tube type, this is not the desired equation for commercial applications. In future, it is desired to have reasonable analytical representations of the true inter-contact thermal conductivity as a function of separation distance, tube type, temperature and defects etc.

3.1.6 Thermal Model Implementation

A random value for length, diameter, chirality, orientation, and spatial location is sampled from their respective distributions. This process is repeated until the representative element is filled to the desired volume fraction in accordance with the Equation (3.3). Then appropriate periodic boundary conditions are applied to the representative element. From the planar assumption it is assumed that no heat flows through the top or the bottom surfaces, thus a parallel network of planar layers of nanotubes compose the entire cnt thin film. Each parallel layer is considered identical, with the thermal transport constrained within each plane, thus the conductivity of a single layer is equivalent to the conductivity of the entire network. For the periodic boundary conditions defined, the conductivity of the layer is equivalent to the conductivity of the representative element (see e.g., [8, 47] for a discussion of the mathematically identical electrical network). Thus, the effective thermal conductivity of the representative element, and by extension the entire network, can readily be obtained from the classical definition for conductivity [44] as follows.

To compute the effective thermal conductivity the model selects the representative element as discussed, and applies a thermal potential ΔT between the $x_1 = -h_1$ and $x_1 = h_1$ edges of the representative cell and the temperature drop is given as

$$\Delta T = T_2 - T_1 \tag{3.16}$$

The representative element's thermal resistance as given by :

$$R_{RE} = \frac{2h_1}{2h_2\, t\, \kappa_{RE}} \tag{3.17}$$

The effective conductivity of the representative element κ_{RE} is given by:

$$\kappa_{RE} = \frac{2h_1}{2h_2\, t\, R_{RE}} \tag{3.18}$$

where $2h_1$, $2h_2$ and t are, respectively, the longitudinal length of current travel, the length perpendicular to current travel and the thickness of the representative element. For an individual layer the resistance, R_{Ω_i}, is given as:

$$R_{\Omega_i} = \frac{L_1}{\kappa_{RE}\, t\, L_2} = R_{RE}\frac{2h_2\, t\, L_1}{2h_1\, t\, L_2} = R_{RE}\frac{h_2\, L_1}{h_1\, L_2} \tag{3.19}$$

where where L_1 and L_2 are, respectively, the width and the depth of the representative element, L_3 is the thickness of the sample shown in Figure 3.7. The model assumes the current flow to be planar, hence the effective resistance of the network R_N is simply that of parallel resistors as depicted in Figure 3.7 and is given as:

$$R_N = \left(\sum_{i=1}^{N_L}\frac{1}{R_{\Omega_i}}\right)^{-1} = \left(\sum_{i=1}^{N_L}\frac{1}{R_{\Omega}}\right)^{-1} = \frac{1}{R_{\Omega_i}}\left(\sum_{i=1}^{N_L}1\right)^{-1} = \frac{R_\Omega}{N_L} \tag{3.20}$$

Assuming the resistance of each layer is constant we have

$$R_\Omega = R_{\Omega_i}, \forall\, i \in \{1, 2, ..., N_L\} \tag{3.21}$$

Combining Equations 3.17-Equations 3.21 we get the effective conductivity of the entire network κ_N as:

$$\kappa_N = \frac{L_1}{R_N\, L_2\, N_L\, t} = \frac{N_L\, L_1}{R_\Omega\, L_2\, N_L\, t} = \frac{2h_1\, L_1\, L_2}{R_{RE}\, 2h_2\, L_2\, L_1\, t} = \frac{2h_1}{R_{RE} 2h_2\, t} = \kappa_{RE} \tag{3.22}$$

It can be clearly seen that the conductivity of the entire sample is equivalent to the conductivity of the representative element given in Equation (3.18).

$$\kappa = \kappa_{RE} = \frac{L_1}{L_2\, L_3}\frac{1}{R_{RE}} = \frac{L_1}{L_2\, L_3}\frac{2h_2\, t\kappa_{RE}}{2h_1} \tag{3.23}$$

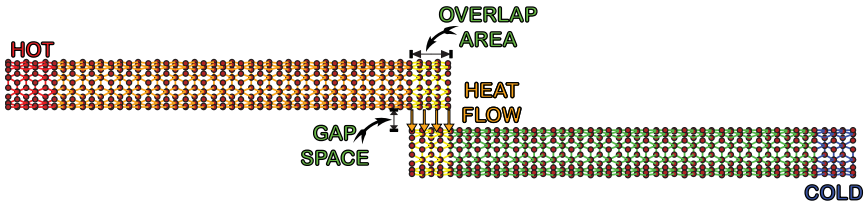

Figure 3.5: Typical thermal element between two nanotubes.

where L_1 and L_2 are, respectively, the width and the depth of the representative element, L_3 is the thickness, The steps in performing the analysis can be summarized through the following algorithm:

1. Construct a representative element with each planar dimension sufficiently larger than the largest geometric feature in consideration.

2. Fill the representative element with nanotube bundles sampled from their respective stochastic distributions for bundle length, bundle diameter, spatial position chirality, spatial orientation, and for tubes that geometrically overlap the separation distance.

3. Impose the geometric periodic boundary conditions.

4. Retain the points of inter contact, and sample the inter-contact resistance.

5. Calculate the elemental conductance K matrix based on the information above. (Detailed discussion in Chapter Four.)

6. Apply a thermal load in the x_1 direction, measure the temperature drop, and compute the bulk thermal conductivity in the direction of flow of heat.

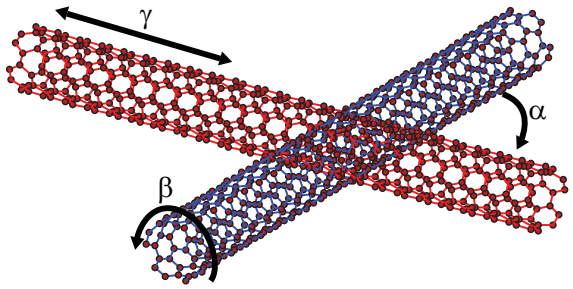

Figure 3.6: Registry Response Surface.

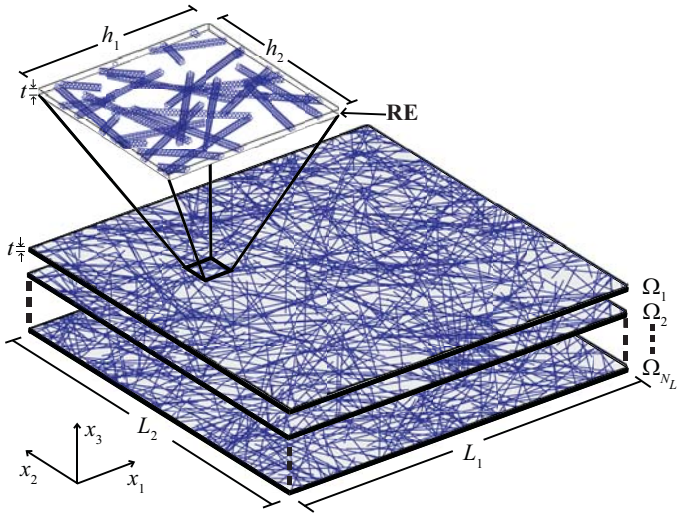

Figure 3.7: CNT Thin Film Network.

3.1.7 Model Validation

It is desired to validate our model against available experimental data from the literature. Unfortunately, the availability of a single inclusive study with reasonable knowledge of the input distributions is yet to be found. Observations have been made from SEM imaging of nanotube bundle diameters and lengths, and it was concluded that they could be reasonably represented through a two parameter Weibull distribution (see e.g., [1]) with $\alpha \in (0, \infty)$ and $\beta \in (0, \infty)$, with the independent

variable $x \in (0, \infty)$ as

$$W(x, \alpha, \beta) = \beta \alpha^{-\beta} x^{\beta-1} e^{-\left(\frac{x}{\alpha}\right)^{\beta}} \tag{3.24}$$

where the parameter α has the same units as the independent variable x. The best fit values for the Weibull distribution from Yeh [1] for the length and diameter distributions are $d_i \in W(x, 13.52nm, 2.84)$ and $L_i \in W(x, 2.03\mu\text{m}, 1.91)$. Unfortunately, these numbers are valid only for her unique samples, but as we will be comparing our results to the thermal results available from the same research group it is anticipated the fabricated samples may have similar length and diameter distributions. The results from Yeh for length and diameter occur several years after the work of Gonnet *et al.* [22] thus we anticipate that her results will overpredict the nanostructural makeup of the network, and we will over predict the bulk conductivity.

Gonnet *et al.* [22] performed a study of the thermal conductivity of planar carbon nanotube networks as a function of temperature, and loosely, the orientation. Their results do not provide any discussion of the nanostructure characteristics, such as nanotube length, diameter, orientation distribution function, nanotube types, etc. We will assume a volume fraction of 60% as alluded to in Gonnet *et al.* [22]. The presented model is exercised with a unit cell thickness of 5nm $\mu_d/3$ and a cell width and depth of $10 \times \mu_l$. The resulting thermal conductivity from over 200 simulations is 37.4 ± 1.4W/(mK). This is quite close to the measured value of 20 W/(mK) by Gonnet*et al.* [22]. The biggest contributor to the discrepancy is attributed to the uncertainty in the length and diameter values between those used in the model simulation and the actual experimental system. The model dependence on length and diameter distribution has been shown using case studies in chapter Five.

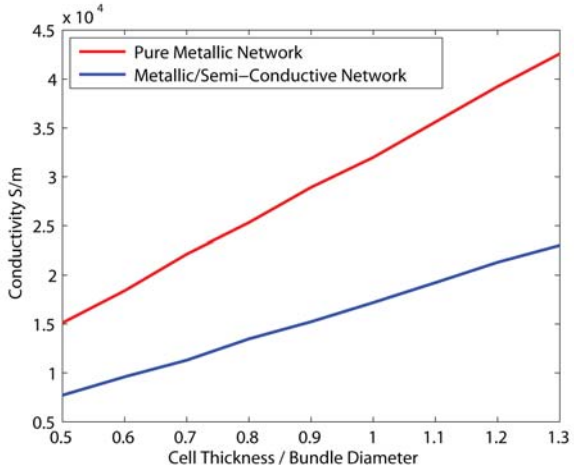

Figure 3.8: Electrical conductivity as a function of cell thickness.

3.2 Limitations of 2D Model

The thermal model was based on the electrical model presented in [44] as discussed for thermal model, electrical model also constraints the orientation of each tube to lie within a single plane but the center of mass of the tubes to vary in any direction. The tubes are also assumed to be longitudinally rigid, with small local deformation occurring in the transverse direction. The network for electrical model is also exposed to air which is an insulator compared to the tube intrinsic resistance. The model assumes that Kirchhoff's law for carrier transport in the linear regime is valid and there is continuity of current without any system leakage. In other words, if s is the direction of flow of thermal current along the tube, then:

$$\frac{dI}{ds} = 0 \tag{3.25}$$

I represents the current. Hence, the electrical potential function ϕ between the tubes is the only consideration and is governed by the constitutive equation:

$$\frac{\partial^2 \phi}{\partial \hat{x}^2} = \beta_{ij} \left(\tilde{I}_i - \tilde{I}_j \right) \tag{3.26}$$

where $\hat{x}^2$ is a point in space between the i^{th} and j^{th} tubes, respectively, and β_{ij} is the charge transfer coefficient between the tubes. The electrical conductivity of the representative element for electrical model is given by:

$$\sigma_{RE} = \frac{L_1}{R_{RE} L_2 t} \tag{3.27}$$

The electrical model uses a similar approach as discussed for the thermal model to predict the electrical conductivity (see [44] for detailed discussion).

A true 2D model assumes zero or negligible cell thickness, which is not the case in real world. It is therefore necessary to quantify appropriate cell thickness L_3 or cell height even for evaluating the 2D planar network. Yeh [1] selected the cell height to correspond to the maximum nanotube diameter sampled from the weibull distribution and a similar assumption was made in [8]. This was based on the assumption that the plane of tubes in a sheet somehow correspond to the proper accounting of tubes within the 2D volume(see e.g. [1,8])which was never validated. This assumption was made with the recognition that the choice of the cell width should have no bearing on the resulting conductivity of the network.

To investigate the validity of this assumption, a study was presented in [41], samples were generated within the representative area element of width $L_1 \geq 10 \times \mu_l$ and $L_2 \geq 10 \times \mu_l$ and the height

$$\frac{1}{2} t' \leq L_3 \leq \frac{3}{2} t' \tag{3.28}$$

where $t' = \mu_d$ or $t' = max_{1,2,\ldots,N_f} d_i$. This is equivalent to placing in $\mathbb{R}^2$ rods of a given length l_i within the element, and continuing to pile them on top of each other until a sufficient quantity has been placed in the sample area element to satisfy the volume fraction requirement of Equation (3.1). If the cell height does not alter

the resulting conductivity, the results should be independent of L_3. Using the algorithm for electrical conductivity discussed above and in [8] the representative area elements are constructed for varying thicknesses for both a pure metallic network and a metallic/semi-conductive network. As observed in Figure 3.8 the conductivity for both networks increases with increasing element thickness, thus for a pure 2D network the conductivity is a function of the cell thickness, which violates the 2D assumption.

The failure of this volume argument is due to the fact that as the thickness of the sample is increased, more tubes are placed on the existing tubes in the network, thereby increasing the number of contacts along a single tube. Eventually, as the thickness increases to infinity, the number of contacts of a single tube will increase to infinity as well, which is in direct contradiction to the physical system. The number of tubes was tabulated for each value of thickness for the above example. It was found that for $t = \frac{\mu_d}{2}$ there were 23 ± 8 contacts along each tube and in the case of $t = \frac{3\mu_d}{2}$ there were 59 ± 18 point of contacts along each tube. This increasing number of contacts along an individual tube is not only without physical reason, but will drastically alter the actual conductivity.

3.2.1 Modification of 2D Model

It is therefore necessary to reinvestigate the implementation approach of the original planar assumption whereby all the tubes are assumed to lie in the same plane. The alternative proposed in [41], is to assume tubes have an orientation that is constrained to lie in the plane, but their spatial location can be fully three dimensional. This is equivalent to laying a sheet of nanotubes within a plane, and then laying each sheet on each other in parallel. Each sheet is constructed such that the number of tubes within the element will be equivalent to the desired volume

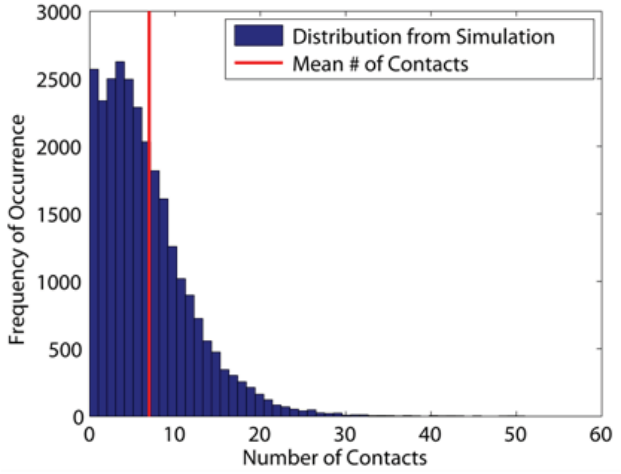

Figure 3.9: Histogram of contacts for the network from the table with $m = 10$, and $n = 100$.

fraction, but there is no requirement that the diameter of a given tube must be fully contained within its selected sheet. In other words, a nanotube's central axis is constrained to be in the representative element, but the entire volume of the tube itself is not necessarily contained within the representative element.

As an initial trial for the method for relating the number of contacts from the three dimensional network to an effective two dimensional planar network, the representative volume element's thickness is reduced until there is a similar number of average contacts per bundle in the two dimensional network as there is in the three dimensional network. As a preliminary study, a two dimensional isotropic network is constructed with a thickness of $L_3 = 0.35\mu_d$ and was found to have 16 ± 6 contacts with the frequency histogram presented in Figure 3.9.

The mean number of contacts from the new simulation is similar to the mean of the planar distribution with $n = 100$, but there is a significant difference in the nature of the contact distribution's spread as observed in Figure 3.10. The results from the 2.5D simulation using the current generation of the in-house developed software for

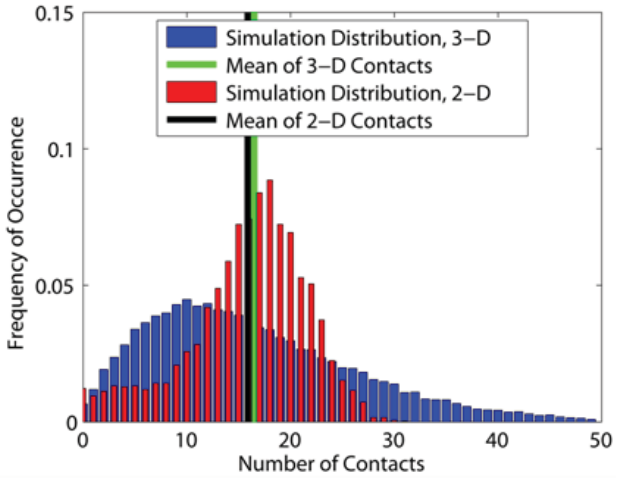

Figure 3.10: Histogram of contacts from the equivalent 2D network and compared to the network from the table with $m = 0$, and $n = 100$.

$L_3 = 0.35\mu_d$ yields a conductivity of 9.8×10^3 S/cm for a pure metallic network and 4.7×10^3 S/cm for a metallic/semi-conductive network, respectively, factors of 2/7 and 3/11 that of the previous version where the thickness was set equal to the mean diameter.

These final numbers are much closer to the desired conductivity values observed experimentally but new issues have been uncovered. It would be more appropriate to develop a 3 dimensional network, hence we abandoned the two dimensional approximation and start focusing on developing a fully three-dimensional network thus avoiding the planar approximation entirely. Next chapter discusses the 3D model, but as demonstrated in [47] the computational requirements will increase exponentially.

CHAPTER FOUR

3D Model

The 3D model is a modification of the 2D model presented in the previous chapter. As demonstrated in chapter 3, the 2D model has the inherent issue of how to choose the appropriate cell thickness, as well as losing the stochastic nature of the frequency of contacts, which prepares ground for the development of fully developed 3D model. The 3D model, as was the 2D model, is based on the idea that, the overall resistivity of a thin film network can be divided into three parts:

1. Resistivity along a nanotube.
2. Resistivity between individual nanotubes.
3. Resistivity between the thin film network and surrounding media, where in the present context this is air.

As shown in [48] and discussed in Chapter Three, the overall resistance is dominated by the intercontact resistance. Hence, we neglect the other two parameters for resistance calculation.

4.1 3D Model Development

The 3D model uses independent stochastic parameters for the length of a nanotube l_i, diameter d_i, chirality (metallic or semiconducting), and orientation. It also uses stochastic distributions for the intercontact resistance and the tube-tube separation distance from the MD simulation results. As shown in Figure 4.1, a 3D sample, consists of layers of thin films. For the current study, we have constrained the orientation of each tube to lie within a single plane, but the center of mass of the

tubes can vary in any of the three directions [44]. The matrix around the network is air, which effectively is an insulator compared to the intrinsic resistance of the tube. The intrinsic resistance of the individual tubes is several orders of magnitude less than the inter-contact resistance between tubes as shown in [48]. Hence, for this model also we will neglect this resistance. Another assumption for the model is the continuity of flow (flow meaning thermal heat flow for the thermal model and electric current for electrical model), with the only discontinuity occurring at the point of contact. Defining s as the direction along the tube, this assumption is equivalent to stating:

$$\frac{dQ}{ds} = 0 \tag{4.1}$$

and

$$\frac{dI}{ds} = 0 \tag{4.2}$$

along each tube. Here Q and I represent the thermal and the electrical flow respectively. Hence, the potential function between the tubes is the only consideration. For the thermal system, the potential function is $\psi = T - T_o$ where, T_o is reference temperature, and for the electrical system $\Phi = V - V_o$ where the reference temperature V_o is typically taken as ground. This potential function is governed by the constitutive equation [49]

$$\frac{d^2\psi}{d\tilde{x}^2} = \alpha_{ij}\left(\psi_i - \psi_j\right) \tag{4.3}$$

$$\frac{d^2\Phi}{d\tilde{x}^2} = \beta_{ij}\left(\Phi_i - \Phi_j\right) \tag{4.4}$$

where ψ and Φ are the potentials at a given point in space $\tilde{x}$ between the i^{th} and the j^{th} tubes for thermal and electrical systems, respectively. ψ_i, ψ_j and Φ_i, Φ_j are

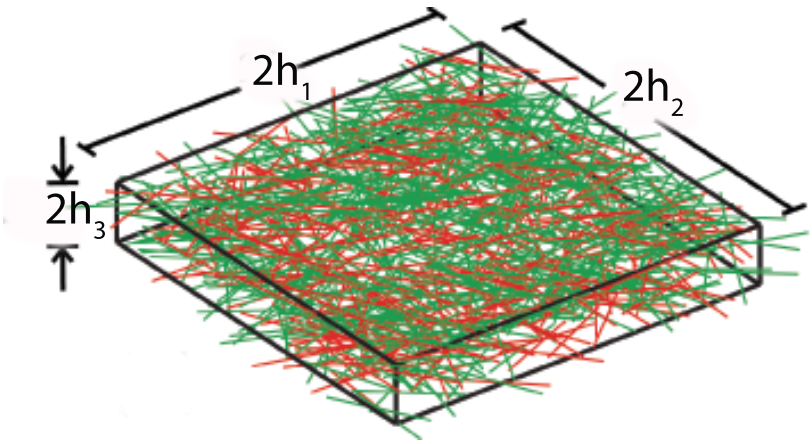

Figure 4.1: Carbon nanotube network schematic.

respectively the potentials at i^{th} and j^{th} tubes for thermal and electrical systems, respectively. α_{ij} and β_{ij} are the coefficients of transfer for the thermal and electrical current respectively, which are related to the contact resistance [43, 44].

For the second order, one dimensional, partial differential equation for temperature with constant coefficients Equation (4.3) reduces to (3.7) (Fourier's Law) as presented in [45] in previous chapter. Similarly Equation (4.4) for for the voltage with a constant coefficient β_{ij} may be represented by [45] (Ohm's Law)

$$\frac{1}{R_e}\begin{bmatrix} 1 & -1 \\ -1 & 1 \end{bmatrix}\begin{Bmatrix} V_1^e \\ V_2^e \end{Bmatrix} = \begin{Bmatrix} I_1^e \\ I_2^e \end{Bmatrix} \tag{4.5}$$

where, $1/R_e$ is electrical conductance, V_i^e is the voltage of the i^{th} tube and I_i^e is the current flow passing either out of the 1^{st} tube or into the 2^{nd} tube.

The intercontact resistance ($\frac{A_e k_e}{h_e}$ for the thermal system and R_e for the electrical system) depends on several parameters such as the bundle length L and bundle diameter d, the relative orientation of the tubes, and thus the global orientation of the tubes θ (orientation w.r.t. x_3 axis), for the current studies we assume $\theta = \frac{\pi}{2}$, (i.e. we restrict all the nanotubes to lie in $x_1 - x_2$ plane) and ϕ (orientation of the projection

of the tube in $x_1 - x_2$ plane measured from the x_1 axis), tube chirality C (metallic or semiconducting) and the registry ζ between the tubes [44, 50]. Hence, the complete contact resistance can be thought of as a probability distribution function f as:

$$R_{ic} = f(L, D, \theta, \phi, C, \zeta, h_e) \tag{4.6}$$

where each parameter belongs to their respective stochastic functions and can be sampled using Monte Carlo simulation technique [44, 49, 50]. It is computationally incomprehensible to consider every single tube within the network for conductivity calculations. Hence, we construct a representative element of dimensions $2h_1 \times 2h_2 \times 2h_3$ (see Figure 4.1) such that the following two conditions are satisfied:

1. There is continuity between adjacent elements, implying geometric continuity of the adjacent sides of a given element. In other words a tube exiting one side of the representative element enters the converse edge.

2. The element is large enough to capture the stochastic nature of all geometric and chirality effects, but small enough to be solved on a small scale work station.

Additionally, on a macroscopic scale, the flow (both thermal and electrical) is unidirectional (from source to sink), but within a network on a nanoscale, the flow is along the tubes which are aligned in any direction. Hence, globally the current may be unidirectional, but the local current flows in three dimensions. In order to make sure the representative element satisfies this condition, the bulk flow $I(\mathbf{x})$ for electrical and $Q(\mathbf{x})$ for thermal is constrained to travel from the $-x_2$ direction to the $+x_2$ direction, and the $x_1 = \pm h_1$ and $x_3 = \pm h_3$ edges are boundaries of symmetry, i.e. current passing through the $x_1 = \pm h_1$ edge is mapped to pass through $x_1 = \mp h_1$ boundary with no energy loss and current passing through the $x_3 = \pm h_3$ edge is mapped to

pass through $x_3 = \mp h_3$ boundary with no energy loss. Thus, the electrical current boundary conditions can be expressed as:

$$I(h_1, x_2, x_3) = I(-h_1, x_2, x_3),\ x_2 \in (-h_2, h_2), x_3 \in (-h_3, h_3) \tag{4.7}$$

$$I(x_1, x_2, h_3) = I(x_1, x_2, -h_3),\ x_2 \in (-h_2, h_2), x_1 \in (-h_1, h_1) \tag{4.8}$$

Similar expressions hold for the thermal current Q from the related thermal network, as:

$$Q(h_1, x_2, x_3) = Q(-h_1, x_2, x_3), x_2 \in (-h_2, h_2), x_3 \in (-h_3, h_3) \tag{4.9}$$

$$Q(x_1, x_2, h_3) = Q(x_1, x_2, -h_3), x_2 \in (-h_2, h_2), x_1 \in (-h_1, h_1) \tag{4.10}$$

The boundary condition $x_2 = \pm h_2$ is quite different as it represents the source and sink. The geometric symmetry is still followed but all the tubes touching the $x_2 = -h_2$ side of the element are considered to be at the same potential, Φ_1 for the electrical system and ψ_1 for the thermal system, and all the tubes touching the $x_2 = +h_2$ are considered to be at the same electrical potential Φ_2 or thermal potential ψ_2. For the electrical system the above condition creates a potential drop

$$\Delta\Phi = \Phi_2 - \Phi_1 \tag{4.11}$$

occurring between the boundaries, mathematically represented as:

$$\Phi(h_1, x_2, x_3) = \Phi_1, x_1 \in (-h_1, h_1), x_3 \in (-h_3, h_3) \tag{4.12}$$

$$\Phi(x_1, x_2, h_3) = \Phi_1, x_1 \in (-h_1, h_1), x_3 \in (-h_3, h_3) \tag{4.13}$$

Similarly for thermal system, the boundary condition implies a change in the thermal potential

$$\Delta\psi = \psi_2 - \psi_1 \tag{4.14}$$

occurring between the boundaries:

$$\Psi(h_1, x_2, x_3) = \psi_1, x_1 \in (-h_1, h_1), x_3 \in (-h_3, h_3) \tag{4.15}$$

$$\Psi(x_1, x_2, h_3) = \psi_1, x_1 \in (-h_1, h_1), x_3 \in (-h_3, h_3) \tag{4.16}$$

In order to compute the effective network resistance in the electrical system, an electrical current I is applied at $x_2 = -h_2$ edge of the representative element and the voltage drop, $\Delta\Phi = \Phi_2 - \Phi_1$, between $x_2 = -h_2$ and $x_2 = +h_2$ boundaries is calculated with our in-house parallelized finite element solver with the aforementioned boundary conditions. The electrical resistance of the representative element R_{RE} can be calculated as:

$$R_{RE} = \frac{\Delta\Phi}{I} \tag{4.17}$$

and the effective conductivity of the representative element is simply expressed

$$\sigma_{RE} = \frac{h_1}{2h_2h_3}\frac{1}{R_{RE}} \tag{4.18}$$

It has been shown in [44] that the effective electrical conductivity of the entire sample σ_N for a 2D system is given mathematically by:

$$\sigma_N = \sigma_{RE} \tag{4.19}$$

and as discussed in Chapter Three Equation 3.22

$$\kappa_N = \kappa_{RE} \tag{4.20}$$

and it will be assumed, this relationship holds for the 3D networks as well.

4.2 3D Model Validation

The code for the model is written in two programming languages, MATLAB and FORTRAIN 90. The MATLAB code is used to read the simulation inputs defining

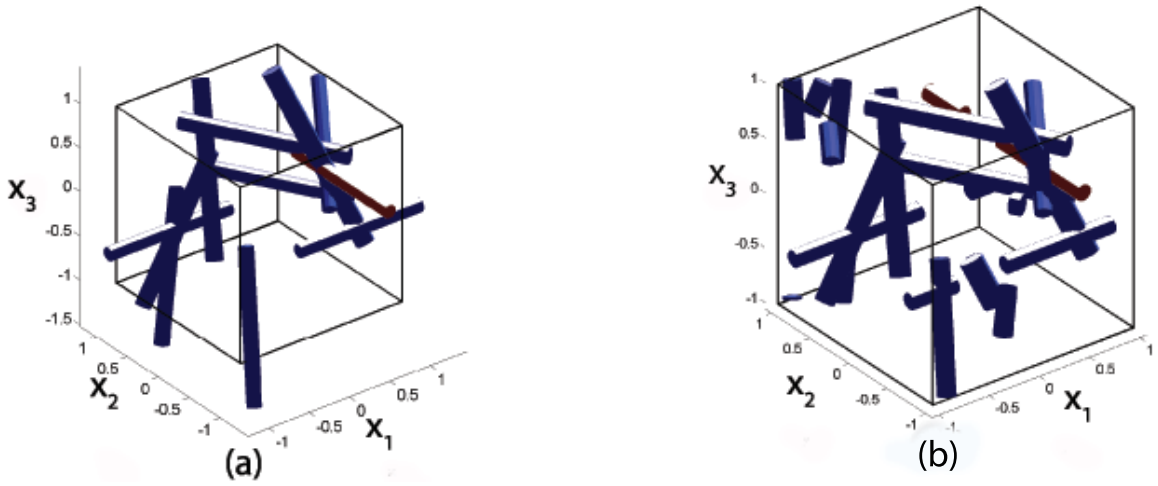

Figure 4.2: Configuration of the CNT Network (a)Before periodicity and (b)After periodicity.

the geometric and the chiral parameters, such as length, diameter, chirality, orientation etc. Based on the inputs, MATLAB generates the initial configuration within the representative element, and applies the periodic boundary conditions to it. The MATLAB code then calls the FORTRAN solver, which in turn assigns nodal resistances, based on chirality of the tubes and computes the overall resistance of the network. The FORTRAN software suite computes the global resistance matrix from the nodal resistances, and uses a sparse PARDISO solver to solve the resulting system of equations. The solution is then returned to MATLAB for post processing, such as generating plots and computing the bulk conductivity from the nodal solutions.

In order to validate the results predicted by the model, we conduct the following validation test. Eleven tubes are placed into the representative cell, of dimensions h_1, h_2 and h_3 as shown in Figure 4.2(a). The tubes were positioned such that each wall of the representative cell was penetrated by at least one tube. Also, some tubes were allowed to pass through multiple wall planes to further ensure proper periodicity. Once the initial configuration was formed, periodic boundary conditions were

applied starting with the x_1 direction, i.e. a tube exiting the $+x_1$ face, reenters on the $-x_1$ face and so on. For instance consider the red tube sticking out of $+x_2$ face in Figure 4.2(a), after application of the periodic boundary conditions, the portion of tube sticking out of $+x_2$ face reenters from $-x_2$ face. Figure 4.2(b) shows the final configuration of the network after applying periodicity on all the sides and by removing all tubes that are not participating in the network current path.

Figure 4.3 presents the step by step application of periodic boundary conditions. As can be seen from Figure 4.3(a), periodicity is first applied at the $+x_1$ edge of the representative element. After proper application of the periodicity on $+x_1$ edge, its converse edge i.e. $-x_1$ edge comes next as shown in Figure 4.3(b). The process is then repeated on $+x_2$, $-x_2$, $+x_3$ and $-x_3$ edges as depicted in the figure. The proper application of periodicity was confirmed by manually constructing the network, and comparing the known results with that of Figure 4.2(b).

In order to calculate the network resistance, only the tubes participating in the network formation are considered, the rest are discarded. Once the final network is formed, (as shown in Figure 4.4(a) and (b)) electrical potential is applied across the network along the x_2 direction. The potential drop is then recorded across the network and electrical resistivity is calculated using the developed software suite and also by hand for the equivalent network shown in Figure 4.5.

The model assigns the intercontact resistance to the nodes based on the input information like the chirality and the intercontact distance of the overlapping tubes as seen from Figure 4.4(a)and (b). The location and the magnitude of the resistances were obtained from the output files. An equivalent circuit diagram was constructed based on this information. For example in Figure 4.4(b), consider resistance 14 (R_{14}), in the top left corner, located between nodes 1 and 9. Correspondingly, in Figure 4.5,

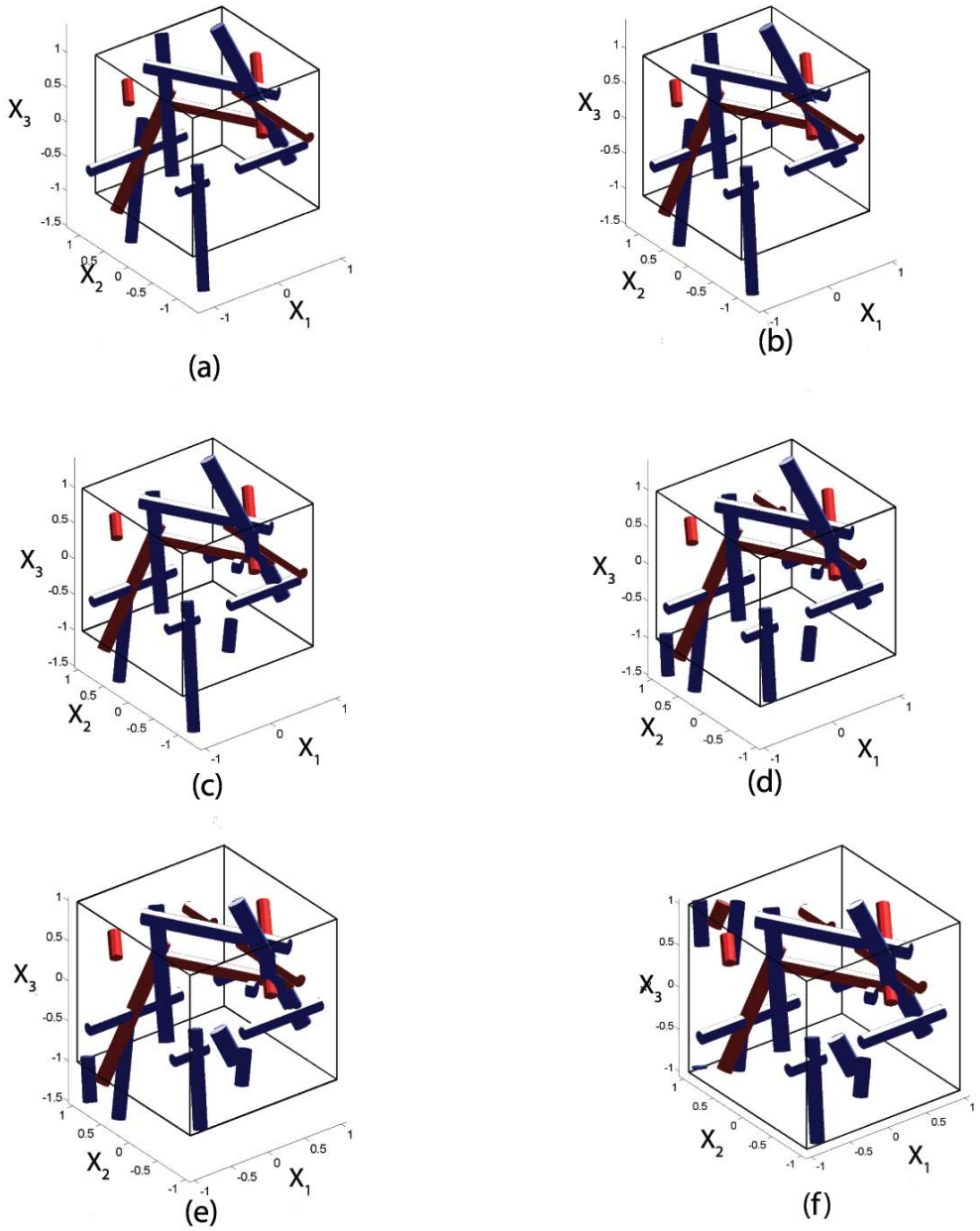

Figure 4.3: Representative element after application of periodic boundary conditions on (a)$+x_1$ edge, (b)$-x_1$ edge, (c)$+x_2$ edge, (d)$-x_2$ edge, (e)$+x_3$ edge and (f)$-x_3$ edge.

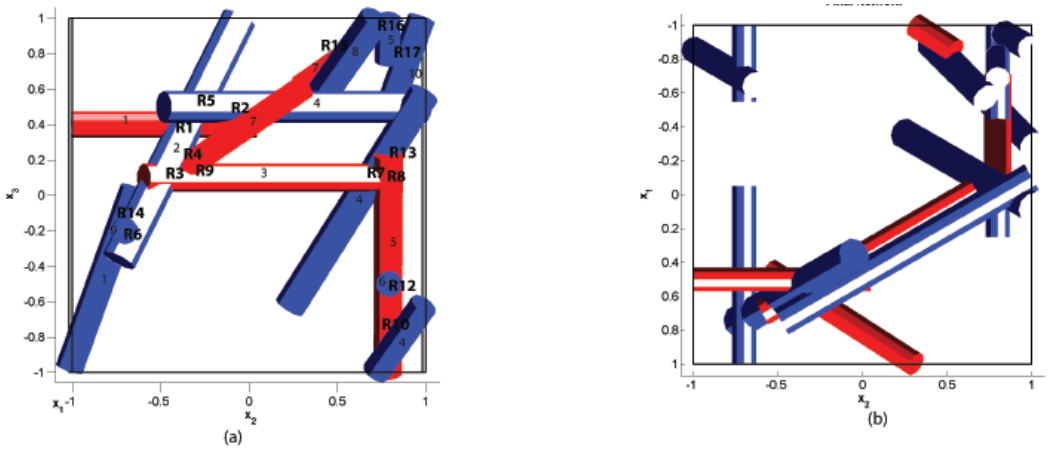

Figure 4.4: Final network after removal of tubes not participating in the network formation (a)Front view and (b)Top view.

resistance R_{14} is the positioned between nodes 1 and 9. This electrical circuit was then solved using the approach discussed below to determine the bulk resistance.

In order to test the validity of this result, the equivalent circuit model for the final network was hand drawn and solved as shown in Figure 4.5. A 1D electrical form of Ohm's Law can be described by the Equation (4.4). For the entire network, it can be represented in its general form as [45]

$$\mathbf{K}V = I \tag{4.21}$$

Where $\mathbf{K}$ represents the nodal conductance matrix, V represents the nodal voltage vector and I represents the nodal current vector. For a network with n nodes, $\mathbf{K}$ is an $n \times n$ matrix, whereas V and I are $n \times 1$ vectors. Matrix $\mathbf{K}$ is formed such that each cell contains its respective nodal conductance, entries are made as the reciprocal of the resistance from the circuit shown in Figure 4.5. For example consider R_{14} again, its location is between nodes 1 and 9 as seen in Figure 4.4(b), its position in the matrix $\mathbf{K}$ (4.23) is at the intersection of 1^{st} row and the 9^{th} column. The matrix $\mathbf{K}$ 4.22, 4.23, 4.24 was constructed in a similar way using all the resistances.

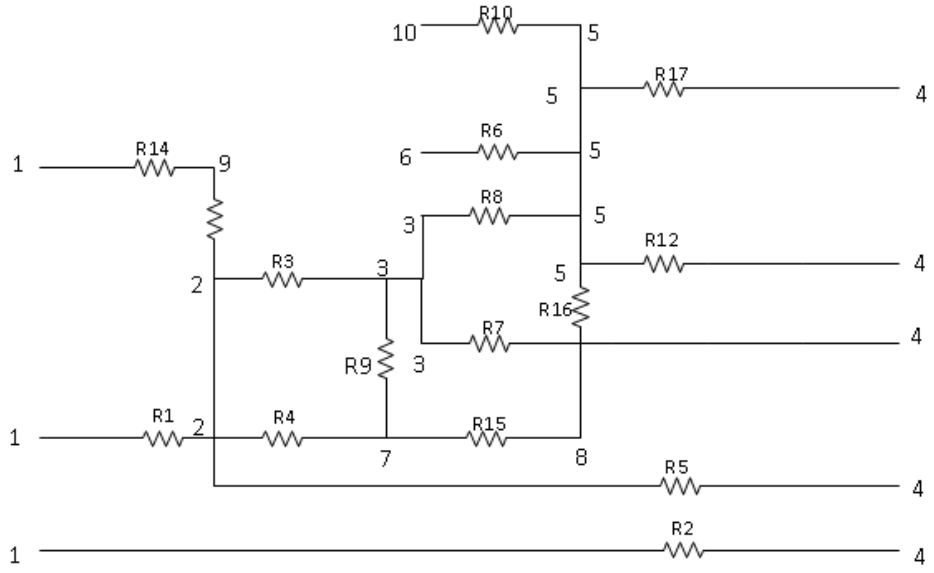

Figure 4.5: Equivalent circuit representation of the CNT network.

$$\mathbf{K}(:,1-3) = \begin{bmatrix} \frac{1}{R_1}+\frac{1}{R_2}+\frac{1}{R_{14}} & -\frac{1}{R_1} & 0 \\ -\frac{1}{R_1} & \frac{1}{R_3}+\frac{1}{R_4}+\frac{1}{R_5}+\frac{1}{R_6} & -\frac{1}{R_3} \\ 0 & -\frac{1}{R_3} & \frac{1}{R_3}+\frac{1}{R_7}+\frac{1}{R_8}+\frac{1}{R_9} \\ -\frac{1}{R_2} & -\frac{1}{R_5} & -\frac{1}{R_7} \\ 0 & 0 & -\frac{1}{R_8} \\ 0 & 0 & 0 \\ 0 & -\frac{1}{R_4} & -\frac{1}{R_9} \\ 0 & 0 & 0 \\ -\frac{1}{R_{14}} & -\frac{1}{R_6} & 0 \\ 0 & 0 & 0 \end{bmatrix} \tag{4.22}$$

$$\mathbf{K}(:,4-5) = \begin{bmatrix} -\frac{1}{R_2} & 0 \\ -\frac{1}{R_5} & 0 \\ -\frac{1}{R_7} & -\frac{1}{R_8} \\ \frac{1}{R_2}+\frac{1}{R_5}+\frac{1}{R_7}+\frac{1}{R_{10}}+\frac{1}{R_{13}} & -\frac{1}{R_{10}}-\frac{1}{R_{13}} \\ -\frac{1}{R_{10}}-\frac{1}{R_{13}} & \frac{1}{R_8}+\frac{1}{R_{10}}+\frac{1}{R_{12}}+\frac{1}{R_{13}}+\frac{1}{R_{16}}+\frac{1}{R_{17}} \\ 0 & -\frac{1}{R_{12}}-\frac{1}{R_{13}} \\ 0 & 0 \\ 0 & -\frac{1}{R_{16}} \\ 0 & 0 \\ 0 & -\frac{1}{R_{17}} \end{bmatrix} \tag{4.23}$$

$$\mathbf{K}(:, 6-10) = \begin{bmatrix} 0 & 0 & 0 & -\frac{1}{R_{14}} & 0 \\ 0 & -\frac{1}{R_4} & 0 & -\frac{1}{R_6} & 0 \\ 0 & -\frac{1}{R_9} & 0 & 0 & 0 \\ 0 & 0 & 0 & 0 & 0 \\ -\frac{1}{R_{12}} - \frac{1}{R_{13}} & 0 & -\frac{1}{R_{16}} & 0 & -\frac{1}{R_{17}} \\ \frac{1}{R_{10}} + \frac{1}{R_{13}} & 0 & 0 & 0 & 0 \\ 0 & \frac{1}{R_4} + \frac{1}{R_9} + \frac{1}{R_{15}} & -\frac{1}{R_{15}} & 0 & 0 \\ 0 & -\frac{1}{R_{15}} & \frac{1}{R_{15}} + \frac{1}{R_{16}} & 0 & 0 \\ 0 & 0 & 0 & \frac{1}{R_6} + \frac{1}{R_{14}} & 0 \\ 0 & 0 & 0 & 0 & \frac{1}{R_{17}} \end{bmatrix} \tag{4.24}$$

For the voltage vector V, initially, all the cells except the 1^{st} which represents the high and 4^{th} which corresponds to the ground are set to 0V. For computational convenience, the low voltage is also set to 0V. Similarly, for the current vector I, though the choice of current is immaterial, for the ease of computation, we assume that the corresponding voltage drop, at the nodes 1 and 4 causes a current of magnitude 1 Amps to flow between the nodes. Hence, as seen in vector I, we have 1 Amps and -1 Amps at the first and fourth rows, respectively. With this initial setup, Equation (4.21) was then solved for unknown source voltage (high) as:

$$V = \mathbf{K}^{-1} I \tag{4.25}$$

This unknown voltage also represents the change in voltage ΔV across the network (low being 0V). With I being the electric current, the overall resistance of the network is calculated as:

$$R_{RE} = \frac{\Delta V}{I} \tag{4.26}$$

For this network the resistance value calculated was 1.18×10^{-6}, which was the same as computed from the developed software thus providing confidence in the proper software implementation of the theory.

$$\mathbf{V} = \begin{bmatrix} V_1 = \text{High} \\ V_2 \\ V_3 \\ V_4 = \text{Low} \\ V_5 \\ V_6 \\ V_7 \\ V_8 \\ V_9 \\ V_{10} \end{bmatrix} \tag{4.27}$$

$$\mathbf{I} = \begin{bmatrix} I_1 = 1\text{A} \\ 0 \\ 0 \\ I_4 = -1\text{A} \\ 0 \\ 0 \\ 0 \\ 0 \\ 0 \\ 0 \end{bmatrix} \tag{4.28}$$

Thus the implementation of the model was confirmed and and the model assumptions will be validated in Chapter Five. In the next chapter few case studies, especially targeted on the bulk conductivity (both thermal and electrical) dependence on the stochastic nature of the nanostructures are presented.

CHAPTER FIVE

Case Studies

To a design engineer employing CNT thin films for various thermal applications, one of the major concern is the parametric effect of the nanotubes on the bulk thermal and electrical conductivities. Here we present a few parameters which alter the conductivity and which can be controlled by employing proper manufacturing or processing techniques. For example, bundle length and diameter can be altered by sonication etc. Researchers have also been able to successfully orient the nanotubes to a certain extent in a thin film network, using high intensity magnetic field [22]. We first begin with the determination of appropriate dimensions for the representative element.

5.1 Representative Cell Dimensions

Macroscopically a thin film contains millions of nanotubes forming a network. Due to computational capacity constrain, we need to find the RAE (Representative Area Element) or the RVE (Representative Volume Element) of appropriate dimensions that will be small enough so that it can be solved on a small work station while reasonably representing the macroscopic network characteristics. If the representative element dimensions are small relative to the largest geometric feature, the results are suspect. The determination of appropriate cell dimensions for the representative element is crucial for bulk property predictions. In this chapter we present the approach used to determine appropriate cell dimensions for both, 2D and 3D models.

5.1.1 Representative Cell Dimension for 2D Model

Increased element size squares the computational memory requirements, thus reducing the cell size is of significant interest. Simulations were run for various aspect ratios A_r where,

$$A_r = \frac{\mu_l}{\mu_d} \tag{5.1}$$

Here μ_l and μ_d are the mean bundle length and the mean bundle diameter respectively, and Cell width ratio C_w where,

$$C_w = \frac{L_1}{\mu_l} \tag{5.2}$$

L_1 being the width of the cell and we constrain $L_2 = L_1$.

Figure 5.1 shows the plot of thermal conductivity with increasing cell width ratio. It can be clearly seen from the figure, that as the cell width ratio increases the conductivity converges to a constant, that is independent of the cell size. Figure 5.2 shows the plot of relative error as a function of cell width ratio where the error is defined as:

$$err = \left| \frac{\kappa_{maxC_w} - \kappa_{C_w}}{\tilde{\kappa}_{maxC_w}} \right| \times 100\% \tag{5.3}$$

Here, κ_{maxC_w} is the thermal conductivity from the representative element with the cell width ratio of C_w and κ_{C_w} is the best approximation of conductivity taken from the largest available cell size obtained before the computational resources were exceeded. From the plot we can safely conclude that as the cell width ratio approaches $10-13$, the relative error in computing the thermal conductivity is less than 5%. For all the simulations with 2D model we used a cell width ratio of 10.

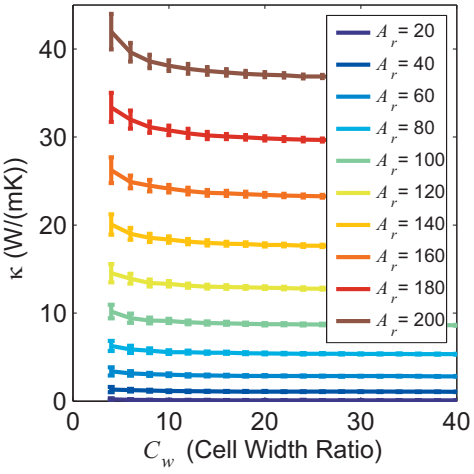

Figure 5.1: Thermal conductivity κ in units of W/(mK) as a function of cell width ratio using 2D Model.

5.1.2 Representative Cell Dimension For 3D Model

To determine the appropriate cell dimensions for the 3D model, we defined the cell width ratio C_w as

$$C_{w,h_1} = \frac{L_1}{\mu_l}, \quad C_{w,h_2} = \frac{L_2}{\mu_l}, \quad C_{w,h_3} = \frac{L_3}{\mu_d}, \tag{5.4}$$

where μ_l is the mean length of the nanotubes and μ_d is the mean diameter. The constraint of the terms h_1/μ_l and h_2/μ_L is made since all tubes are required to lay flat in the $x_1 - x_2$ plane and thus the largest geometric dimension of consideration would be the length. Conversely, the thickness in the x_3 direction h_3/μ_d is chosen to define the cell width ratio as the diameter is the largest geometric parameter of consideration along the x_3 axis.

For various aspect ratios, the thermal conductivity is calculated for a planar isotropic network and the results are shown in Figure 5.3 for various nanotube aspect ratios A_r, where $A_r = L/d$. For each case in the figure, the nanotube diameter is deterministic with a value of 12 nm. The length is then computed from the desired

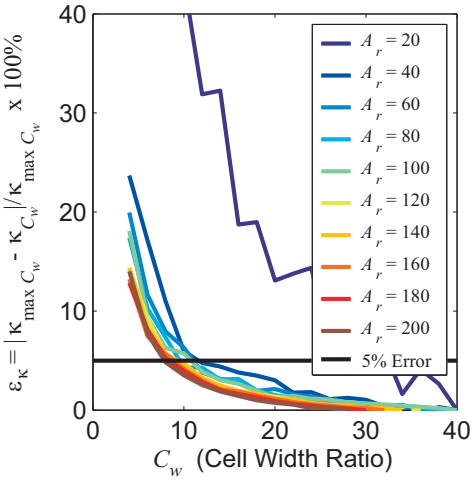

Figure 5.2: Relative error in thermal conductivity as a function of cell width ratio using 2D Model.

aspect ratio and is also constrained to be deterministic. The results in Figure 5.3 are the results for the mean and the standard deviation (designated by the error bars, which are indistinguishable) from at least 500 unique simulations. As can be observed from Figure 5.3 when the cell dimensions used for simulations are too small, the conductivity tends to be overestimated for the 3D model. From the figure it is unclear at what cell width ratio the cell is big enough to accurately capture the bulk conductivity. For the low aspect ratio network this point appears at a much larger cell width ratio than for the larger aspect ratio network. Figure 5.4 shows the plot of relative error as a function of the cell width ratio for the 3D network, here the error is defined as (5.3).

From Figure 5.4 it is observed for the higher aspect ratio nanotubes, the relative error percentage drops below 1% quite quickly and for the case of the aspect ratio of 80 this point occurs around a cell width ratio of 10.

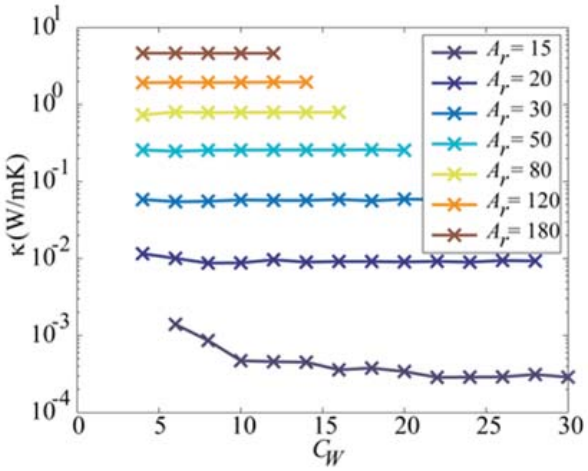

Figure 5.3: Thermal conductivity κ in units of W/(mK) as a function of cell width ratio using 3D Model.

5.1.3 Representative Cell Construction Summary

The following algorithm summarizes the element construction and the ensuing conductivity prediction:

1. Construct a representative element with each planar dimension sufficiently larger than the largest geometric feature in consideration.

2. Fill the representative element with nanotube bundles sampled from their respective stochastic distributions for bundle length, bundle diameter, spatial position chirality, spatial orientation, and for tubes that geometrically overlap the separation distance.

3. Impose the geometric periodic boundary condition.

4. Retain the points of inter contact, and sample the inter-contact resistance.

5. Compute the bulk thermal conductivity in the direction of the flow.

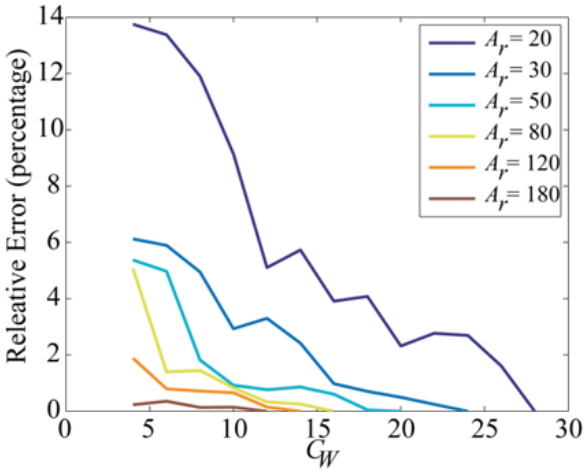

Figure 5.4: Relative error in thermal conductivity as a function of cell width ratio using 3D Model.

5.2 Length Dependence of Conductivity

Bundle length is one of the inputs for the model. This case study investigates the dependence of conductivity on the bundle length and compares the solution with those available in the literature for a similar study [33]. Simulations were performed for both thermal conductivity and electrical conductivity using our 2D and 3D models. For the 2-D study, tubes are placed in a 2-D spatially homogeneous configuration within the sample element and the orientation of each tube is sampled from the 2D planar isotropic distribution,

$$\psi(\phi) = \frac{1}{2\pi} \tag{5.5}$$

which means no θ dependence, i.e.

$$\psi(\theta, \phi) = \frac{1}{2\pi}\delta\left(\theta - \frac{\pi}{2}\right) \tag{5.6}$$

where $\delta(\theta - \frac{\pi}{2})$ is the Dirac delta function that equals zero everywhere except when its argument is zero.

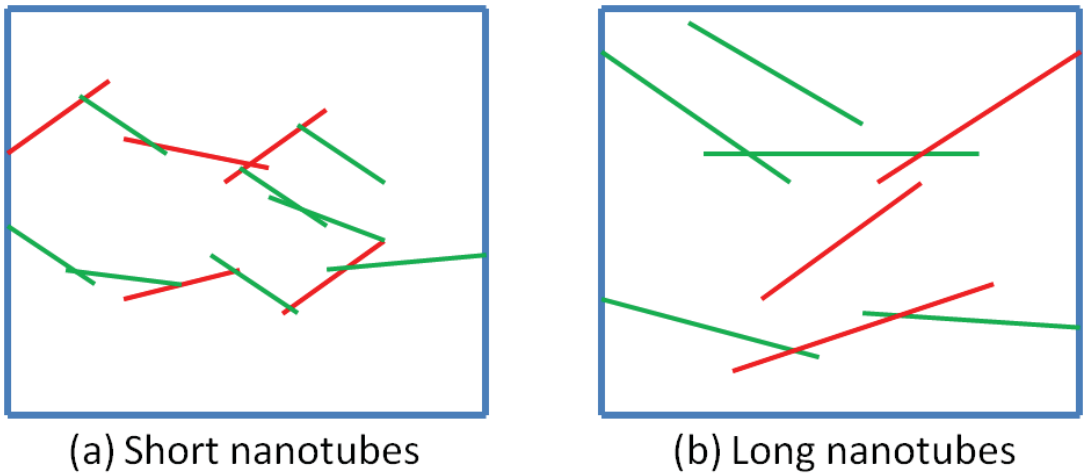

Figure 5.5: Figure depicting the network formation with (a) Shorter naotubes, and (b) Longer nanotubes.

For the 3D study, tubes are placed in a 3-D spatially homogeneous configuration within the sample element and the orientation of each tube is sampled from a 2-D planar isotropic distribution. With increase in bundle length we expect the conductivities (both thermal and electrical) to increase. This is because, with larger tubes, one needs a few tubes to complete the path, i.e., which results in lowering the number of contacts, as shown in Figure 5.5. This results in low resistance.

Results from the simulation were found in agreement with this fact and are discussed in the following subsections.

5.2.1 Thermal Conductivity Dependence on Bundle Length

The dependence of bundle length on the thermal conductivity of a thin film network with a fixed volume fraction is shown using our 2D model in Figure 5.6. These results are for bundles of planar isotropic orientation and bundle lengths varying from 0.3μm to 3μm with a fixed bundle diameter of 10nm. The volume fraction was 60% percent (constant) for all the cases and the the chirality ratio was 1 : 2 for

metallic to semiconducting. Each data point is the mean of 100 runs. It is clear from the figure, that there is considerable increase in the thermal conductivity, with increase in bundle length. Single order of increase in the magnitude of bundle length could lead to two orders of increase in the bulk thermal conductivity.

$$\kappa(L) = 6.74 \times 10^{13} L^{2.16} \tag{5.7}$$

$$\kappa(L) = 8 \times 10^{12} L^{1.868} \tag{5.8}$$

Similar study was done using the 3D model, by fixing the bundle diameter to 10nm and the results are plotted in Figure 5.7. Equations (5.7) and Equation (5.8) are curve fits to the data obtained for the 2D and 3D case. These analytical equations are in S.I. units. From the plot it is clear that conductivity is a direct function of bundle length. Also, for the 3D model we considered two cases, one with the network consisting of entirely metallic nanotubes and other with the mixed chirality i.e. metallic to semiconducting ratio being $1 : 2$. From the plot, it is clear that, the chirality does not have any impact on the bulk thermal conductivity of the network, but it does affect the bulk electrical conductivity, as will be seen in Figure 5.9

5.2.2 Electrical Conductivity Dependence on Bundle Length

The results for the electrical conductivity are plotted in Figure 5.8 for the 2D model which demonstrate a steady increase in conductivity as a function of increasing bundle length, with a best fit power curve given in the figure where L is given in units of micrometers (μm). The study was conducted for a network consisting entirely of metallic tubes and semiconducting tubes. Results show that unlike, thermal conductivity, electrical conductivity depends on the chirality of the nanotubes in the network. Equation (5.9) and Equation (5.10) represent the curve fir for metallic

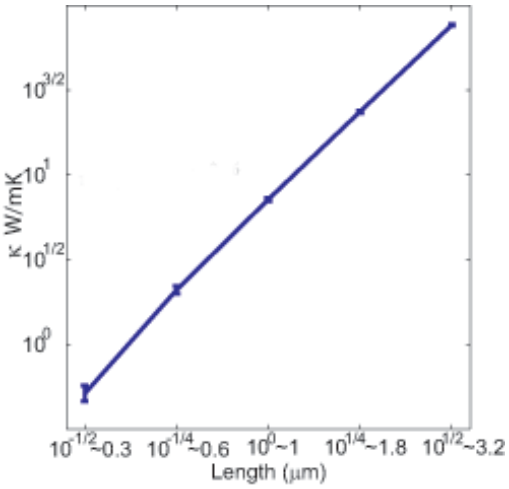

Figure 5.6: Thermal conductivity κ as a function of bundle length using 2D model.

network and a network with mixed nanotubes for 2D case.

$$\sigma(L) = 6.3 \times 10^{15} L^{1.9} S/m \tag{5.9}$$

$$\sigma(L) = 2.3 \times 10^{16} L^{2} S/m \tag{5.10}$$

Figure 5.9 presents the plots for same study from our 3D model. Chirality dependence similar to the 2D model was observed. Equation (5.11) and Equation (5.12) represent the curve fit for metallic network and a network with mixed nanotubes for 3D case.

$$\sigma(L) = 2.76 \times 10^{16} L^{1.9} S/m \tag{5.11}$$

$$\sigma(L) = 2.66 \times 10^{16} L^{1.94} S/m \tag{5.12}$$

These analytical equations are in S.I. units. From these plots we could safely conclude that increasing the percentage of metallic carbon nanotubes would improve electrical conductivity. Hence, the manufacturing process should be directed in this direction.

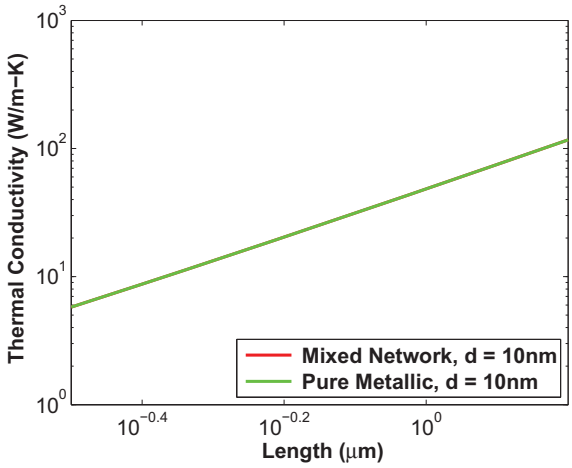

Figure 5.7: Thermal conductivity κ as a function of bundle length using 3D model.

5.3 Diameter Dependence of Conductivity

There have been many attempts to study the dependence of conductivity on diameter. Diameter also being one of the input factors for our model, we here present a case study for conductivity predictions as a function of nanotube bundle diameters ranging from 5nm to 25nm with the same assumptions on orientation, spatial homogeneity, and volume fraction as in the previously discussed conductivity dependence on length study. For all the simulations we selected the length of each nanotube to be 2μm with a volume fraction of nanotubes being 60%. It is clear from all the plots that there exists a nice inverse relationship between the bundle diameter and bulk conductivity. This trend is expected as for a fixed volume fraction, orientation and bundle length, the decrease in the bundle diameter will result in increase in the number of tubes. More tubes provide better alternative paths with least resistance for the flow, as shown in Figure 5.10 hence with the decrease in diameter (or increase in the number of tubes) the resistance decreases thereby increasing the bulk conductivity.

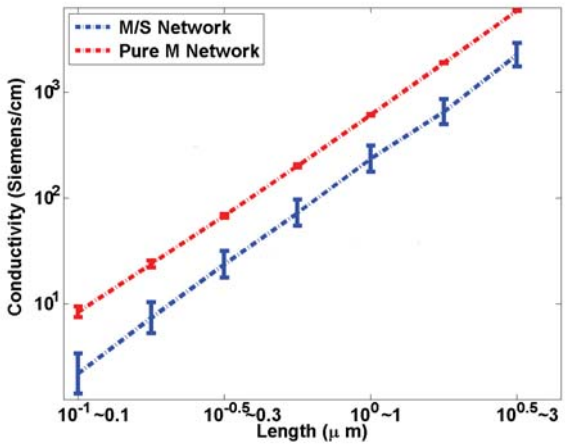

Figure 5.8: Electrical conductivity σ as a function of bundle length using 2D model.

5.3.1 Electrical Conductivity Dependence on Bundle Diameter

In the 2D model scenario depicted in Figure 5.11, the final number of discrete tubes after imposing the geometric boundary conditions was just over $9,600$ for the 5nm samples and $\sim 1,900$ for the 25nm sample, with the former requiring nearly 900 seconds per computational simulation. It is quite clear from Figure 5.11 that there exist a little spread in the predicted results for the metallic network, whereas for the metallic/semi-conductive network there exist a considerable amount of spread. The 3D model results shown in Figure 5.9 demonstrate a similar trend for the exponent of the best fit function as observed in the 2D model, with the primary difference occurring in the pre-multiplying coefficient. As in the previously discussed length dependence study, the error bars are not presented in the 3D case as they would be nearly indistinguishable from the line itself. The final number of discrete tubes for the 3D study after imposing the geometric boundary conditions was just over $29,000$ for the 12nm samples and $\sim 5,800$ for the 60nm sample, with the former requiring nearly 200 seconds per computational simulation. For a network made entirely of

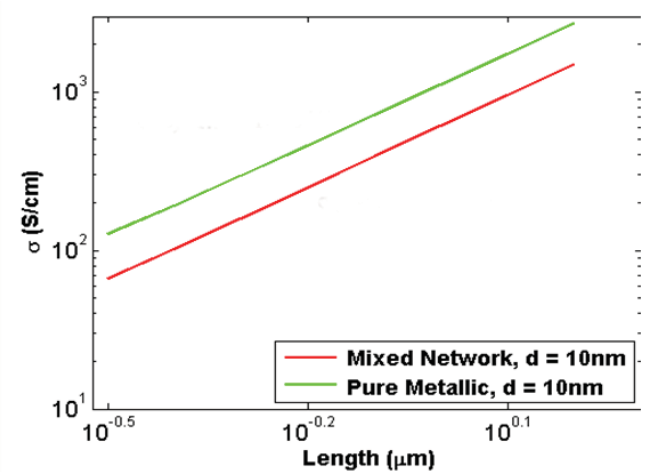

Figure 5.9: Electrical conductivity σ as a function of bundle length using 3D model.

pure metallic carbon nanotubes the electrical conductivity is better, which is inline with the results obtained from length dependent study, discussed earlier. Equation (5.13) and Equation (5.14) represent the curve fir for metallic network and a network with mixed nanotubes for 2D case.

$$\sigma(L) = 2.2 \times 10^{-19} L^{-3} S/m \tag{5.13}$$

$$\sigma(L) = 9.1 \times 10^{-20} L^{-3} S/m \tag{5.14}$$

Equation (5.15) and Equation (5.16) represent the curve fir for metallic network and a network with mixed nanotubes for 3D case. All the analytical solutions are in S.I. units. It is also worthwhile to note that the trends in Figure 5.8 and Figure 5.9, in particular the exponents from the best-fit power law relationship, are similar to the results discussed in Hecht *et al.* [33] where they noted that the exponent would be ~ -2 for perfectly rigid bundles. The discrepancy is attributed to the fact that Hecht *et al.* assumed that each tube would have a single point of contact, whereas in our situation with the 5nm diameter nanotubes an individual nanotube will average

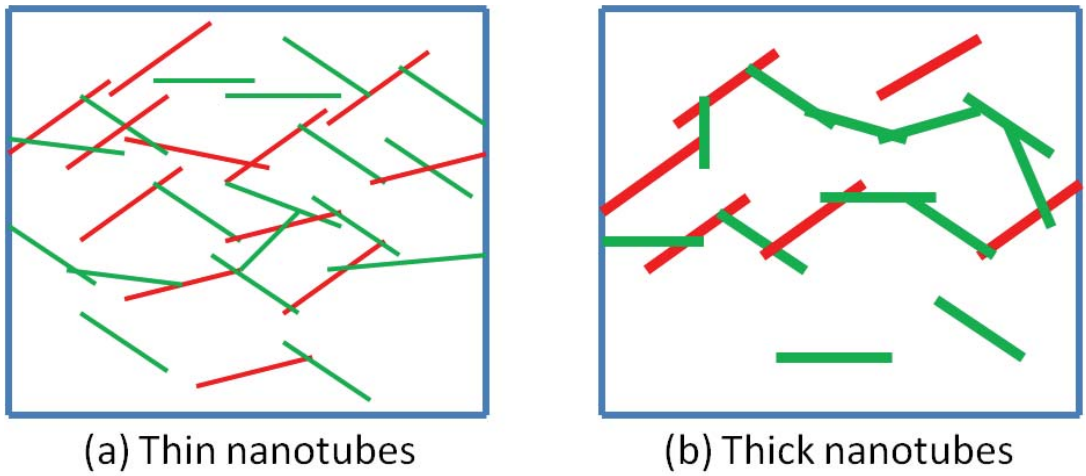

Figure 5.10: Plot depicting two system for same volume fraction, having (a) Thin cabonnanotubes, and (b) Thick carbonnanotubes. It is noteworthy, for a smaller diameter the number of alternative paths across the network are more.

just less than 80 contact points. As in the previous case, there is a considerable gain in conductivity by fabricating a network of purely metallic tubes.

$$\sigma(L) = 3.3 \times 10^{-18} L^{-2.90} S/m \tag{5.15}$$

$$\sigma(L) = 2.0 \times 10^{-18} L^{-2.94} S/m \tag{5.16}$$

5.3.2 Thermal Conductivity Dependence on Bundle Diameter

For a 2D model as depicted by the best fit curve in Figure 5.13, there is a near inverse dependence between conductivity and diameter. Thus an increase in the diameter by a factor of two will result in a decrease in conductivity by a factor of two. Figure 5.14 shows the similar results for the 3D. Equation (5.17) and Equation (5.18) represent the curve fir for the 2D network and the 3D network respectively. It should be noted that chirality does not affect the bulk thermal conductivity of the network.

$$\kappa(d) = 2.6 \times 10^{-7} d^{-1} W/m - K \tag{5.17}$$

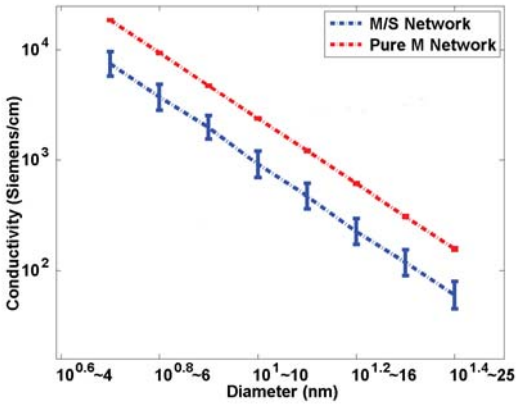

Figure 5.11: Electrical Conductivity as a function of increasing diameter using 2D model.

$$\kappa(d) = 2 \times 10^{-5} d^{-0.869} W/m - K \tag{5.18}$$

5.3.3 Comparison of Thermal Conductivity Dependence with the Electrical Conductivity Dependence on Bundle Diameter

Now let's compare the numerical solutions for the electrical and the thermal conductivity dependence on diameter. From Figure 5.12 above, we can see that the electrical conductivity for a pure network is a function of $\mathrm{d}^{-2.9}$, for thermal conductivity however it is function of $\mathrm{d}^{-0.869}$ as depicted in Figure 5.14. Here is an explanation for this difference. Thermal conductance is given by $\frac{A_e k_e}{h_e}$ as shown in Equation 3.17 where A_e is the cross sectional area of contact, h_e is the separation distance, k_e is the thermal conductivity of the element. The cross sectional area of contact A_e as shown in Equation 5.20:

$$A_e = \frac{D_1 \times D_2}{sin\gamma} \tag{5.19}$$

Where D_1 and D_2 are the diameters of the overlapping tubes and γ is the angle between them. It can be seen from the above relation that for a system with a constant diameter, the area of overlap is directly proportional to the square of the

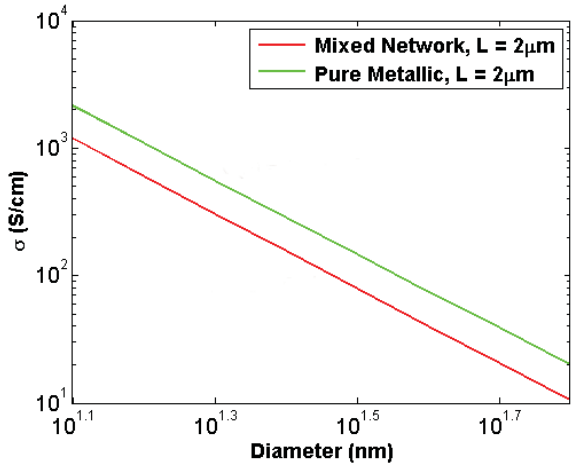

Figure 5.12: Electrical Conductivity as a function of increasing diameter using 3D model.

diameters of the tubes. Hence, the thermal conductivity:

$$\kappa \propto (d^{-2.9})(d^2) = d^{-0.9} \tag{5.20}$$

The above relation explains the discrepancy in the power law for thermal and electrical conductivities.

5.4 Conductivity Dependence on Volume Fraction

The model uses Finite Element approach to calculate the bulk conductivity. A problem with finite element solutions is that, when there is an incomplete network the resulting stiffness matrix will be singular and hence not invertible. In our case an incomplete network occurs below percolation. Hence, the developed algorithm experiences the same limitations, below percolation, but it can still be used for systems just above the percolation threshold. It can be clearly seen from Figure 5.15 that as the network is filled with the tubes just below percolation, the system matrix is invertible and no solution is returned, but once the volume fraction is increased above the percolation threshold a solution for the conductivity is returned.

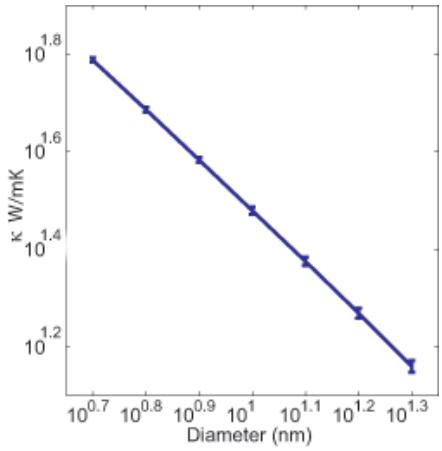

Figure 5.13: Thermal conductivity κ as a function of bundle diameter for 2D model.

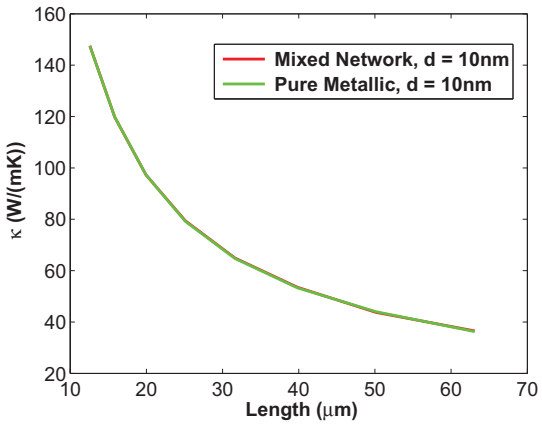

Figure 5.14: Thermal conductivity κ as a function of bundle diameter using 3D model.

A case study is conducted to study the dependence of electrical conductivity on volume fraction. Two different scenarios are considered, for the first setup as can be seen in Figure 5.15 a planar network composed of tubes with a constant length and diameter was considered. It can be seen that for a tube aspect ratio of 40, the percolation threshold occurs for a volume fraction less than 4%, whereas for the aspect ratios of 60 and 80 this occurs for a volume fraction less than 2%. Secondly, the length and diameter were selected from the weibull distribution (3.24) suggested

by Yeh [1]. Figure 5.16 depicts the results obtained for this case. It can be observed from the figure that the percolation volume fraction for the network with stochastic lengths and diameters from the Weibull distribution is observed to occur between 0.5% and 1%.

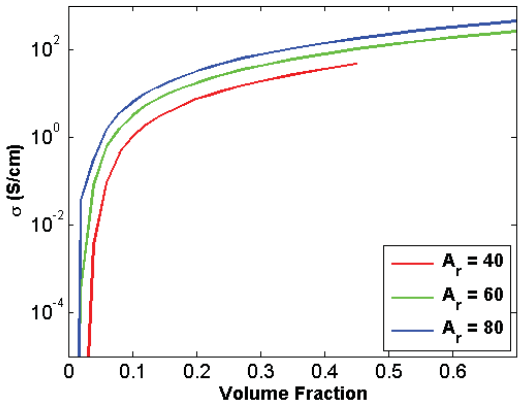

Figure 5.15: Conductivity prediction as a function of bundle volume fraction for fixed length and diameter.

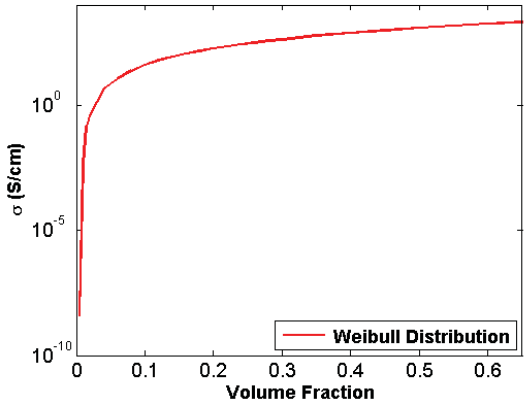

Figure 5.16: Conductivity prediction as a function of bundle volume fraction for length and diameter sampled from the Weibull distribution of Equation (3.24).

It can be seen from the Figure 5.16 that the conductivity increases with increasing volume fraction, with the quickest increases occurring just after the percolation threshold. For the Weibull length and diameter network, the largest volume

fraction studied was 65% and the observed conductivity was $2,030$S/cm. simulating a network with a volume fraction greater than 65%, but this is non-physical as the geometric limitations stating that two tubes must not occupy the same space will prevent a greater packing density for a planar isotropic network. Once the model was validated for proper implementation of the intended logic, we validate the model against the experimental results. Though precise validation of this model is not possible, due to unavailability of accurate information regarding the stochastic input parameters like the bundle length, bundle diameter, chirality ratio and the degree of alignment of the tubes in the network. This is difficult to determine and no research group so far has reported the conductivity values of the thin films along with the information on these parameters. Here we make an attempt to compare the values of the electrical conductivity with that reported in the literature.

To begin with, Park *et al.* [39] who studied the electromagnetic interference shielding properties of carbon nanotube buckypaper composites using carbon nanotube thin films about $10 - 20\mu$m thick, reported that the electrical conductivity of thinfilm of this thickness composed of HiPco SWCNT is 200 S/cm ($20,000$ S/m). In the same work they also presented the electrical conductivity of thin film (thickness $20 - 60\mu$m) consisting of long MWCNT to vary in the range of $400 - 1000$ S/cm ($4 \times 10^4 - 10^5$ S/m). The group further studied the Single-walled carbon nanotube buckypaper and mesophase pitch carbon/carbon composites [40]. In this study they filled in the voids in the thinfilm (thickness 11μ m), consisting of purified HiPco SWCNT by impregnation of pith. They reported that as the voids in the thinfilms decreased due to repeated impregnation cycles, the electrical conductivity rose from 200 S/cm (2×10^4 S/m) to more than 400 s/cm (4×10^4 S/m). The group in another

study on multi-walled carbon nanotube sheet/bismaleimide nanocomposites [38] reported that with increased alignment due to stretching, the electrical conductivity of this thinfilm improves in the alignment direction. They gave the values to vary from 420 S/cm (4.2×10^4 S/m) to 600 S/cm (6×10^4 S/m). The group also reports in their work on mechanical and electrical properties of polycarbonate nanotube buckypaper composite sheets [35] that the average resistivity of a neat thinfilm is about $4.9 \times 10^{-3}\Omega$m which is about same as 200 S/cm (2×10^4 S/m) reported by the group earlier. We basically, rely on the work of this particular group from HPMI, Florida State University, (Fl) for validating our model because; we applied the values reported by Yeh [1] for the length and diameter distributions using high resolution SEM imaging and Gonnet [22]*et al.*'s work provided the information regarding the volume fraction of these thinfilms (about 60%). As, they all came from the same research group; we assume that all the test samples from this group will have the same nanostructure characteristics. Employing the Weibull distribution parameters reported by Yeh [1], for the length and diameter distributions, keeping the volume fraction fixed to 60%, chirality ratio 1 : 3 for metallic:semiconducting, with random alignment the electrical conductivity predicted by the model is 174300 S/m (mean of $20,000$ runs). The values seems high compared to that given by the group, because the model presents an idealized case, with tubes being defect and void free. As discussed above, reduction in voids considerably improves the electrical conductivity. The biggest contributor to the discrepancy is attributed to the difference in the length and diameter values between those used in the model simulation and the actual experimental system. As shown in Chapter Six table 6.6, even a slight change (about 1%) in these weibull parameters, alters the predicted electrical conductivity. Also, the conductivity is also a function of chirality ratio, degree of alignment and volume

fraction. Hence, in order to accurately predict the conductivity, precise information regarding these input parameters is desired.

5.5 Conductivity Dependence on the Degree of Alignment of Tubes

Conductivity of the thin film network is dependent on the relative alignment of the tubes in a network, i.e. it depends on degree of planar orientation of the tubes. It is expected that the more the tubes are aligned along the direction of the flow; the better will be the conductivity. Researchers have been successful in aligning the tubes to a certain extent using high intensity magnetic field [22]. It has been shown by Jack et al. [8] that, the increase in conductivity is shown by the network to a certain degree of orientation, and then the conductivity decreases. In order to study this effect, a case study was conducted with a thin film having a volume fraction of 60%. Three different distributions were selected for length and diameter, namely Weibull, Normal and by keeping the length and diameter constant. The idea behind selecting three different distributions for length and diameter was to test the sensitivity of the model, to the type of distribution selected for the input parameters. The study was done for two scenarios, first the tubes were aligned along the direction of the flow and second the tubes were aligned perpendicular to the direction of the flow.

Simulations to compute the bulk anisotropic conductivity were performed by aligning the tubes along the direction of the current flow through the function

$$\psi(\theta, \phi) = k\delta(\theta - \frac{\pi}{2})cos^{2n}(\phi + \alpha) \tag{5.21}$$

where the coefficient k is selected to satisfy the normalization condition, $\delta(\theta - \frac{\pi}{2})$ is the Dirac delta function that equals zero everywhere except when its argument is zero, and α is a parameter that defines the principal direction of alignment.

Table 5.1: Data used for various distributions.

Parameters	Constant	Normal Distribution		Weibull Distribution	
		Mean	Std Dev.	Mean	Std Dev.
Length	2.2μm	1.8μm	0.78μm	1.8μm	1.8μm
Diameter	12nm	12nm	4.5nm	12nm	4.5nm
Aspect Ratio	185	184		184	
Thickness Ratio	0.45	0.45		0.45	
Cell Width Ratio	15.4	15.4		15.4	

To provide a fair comparison between the various stochastic distributions, the mean and the standard deviation was chosen to be the same. Since the comparison uses the Weibull distribution parameters as given in Equation (3.24) the mean value of the aspect ratio was constrained to be 184 and the mean value of the diameter was 12nm. For each of the three distributions; the mean aspect ratio is the same, as is the standard deviation. Table 5.1 shows the data used for various distributions and the test was conducted on both 2D and 3D models. 50 runs were run for each data point in order to reduce the standard deviation in the data.

5.5.1 Electrical Conductivity Dependence on Orientation

Figure 5.17 shows the conductivity as a function of alignment for various nanotube geometrical distributions for the 3D network. It can be clearly seen from the plot that, the choice of the distribution function will drastically alter the predicted electrical response. Also, it is interesting to note that, the electrical conductivity increases initially with the alignment, and then it drops off with increasing alignment.

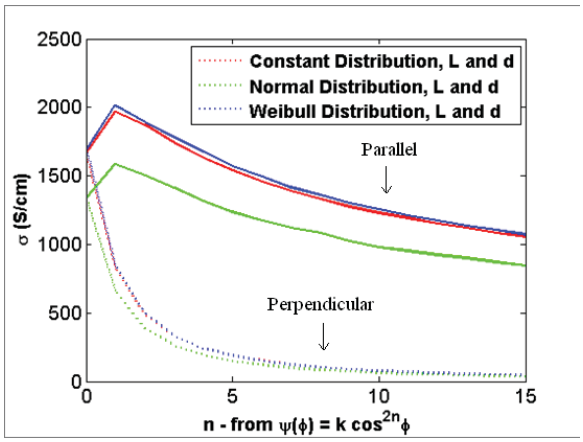

Figure 5.17: Electrical conductivity for select alignment states, as a function of orientation for 3D model.

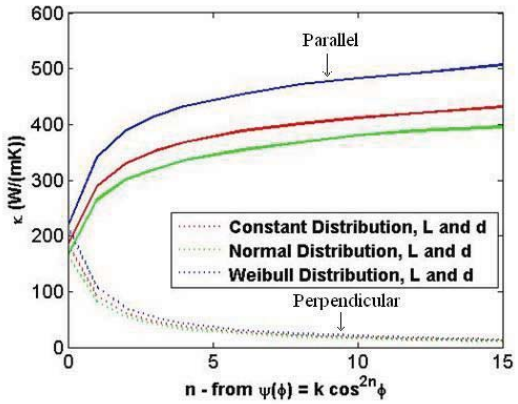

Figure 5.18: Thermal conductivity for select alignment states as a function of orientation for 3D model.

5.5.2 Thermal Conductivity Dependence on Orientation

Similar study was conducted for thermal system. Figure 5.18 shows the conductivity as a function of alignment for various nanotube geometrical distributions for the 3D network. It can be from the figure that there are three distinct plots for three different distributions. Also, the thermal conductivity does not decrease with increase in alignment as is the case with the electrical conductivity.

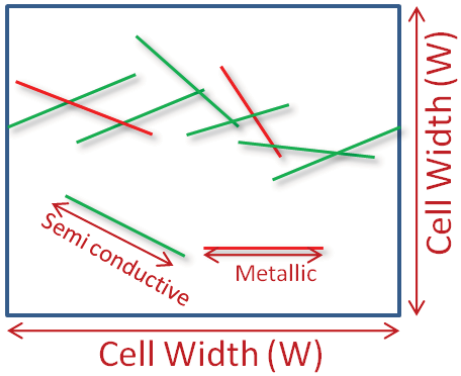

Figure 5.19: Reduced options for networking for individual tubes with increasing alignment.

5.5.3 Difference in the Trends for Thermal and Electrical Conductivities with Increasing Orientation

As can be seen from Figure 5.17 and Figure 5.18 the electrical and the thermal systems behave differently with increasing alignment. Electrical conductivity initially shows an increase, but it then decreases. The rate at which the network conductivity decreases with increasing alignment is expected due to the diminishing networking options for aligned tubes, thus increasing the probability of any given path having as the only option a metallic/semi-conducting intercontact as shown in Figure 5.19.

For a metallic semiconducting contact, the intercontact resistance nearly 2 orders of magnitude greater than a metallic/metallic contact and the semi-conductive/semi-conductive contact. Thermal conductivity on the other hand, shows a gradual increase with alignment, due to the fact, that thermal conductivity is directly proportional to the area of overlap from the relation (3.7). As the tubes get aligned, the area of overlap increases, thereby increasing the thermal conductivity.

CHAPTER SIX

Sensitivity Analysis

Previous chapter discussed the approach used to determine the appropriate dimensions for the representative element. For all the models it was clearly obtained that the conductivity approached to a constant once critical value for the cell width ratio was reached (which was about $10 \sim 13$ for 2D and about $5 \sim 7$ for 3D). This chapter presents two targeted case studies, the first study deals with the dimensional sensitivity of the representative element, while the second study investigates the sensitivity of the thermal and electrical conductivity on the weibull parameters (3.24) of the length and the diameter proposed by yeh [1].

6.1 Representative Element Dimensional Sensitivity Analysis

Unfortunately, due to the rather large computational requirements of a 3D network being nearly two orders of magnitude greater than that of the 2D model, cell dimensions could not be arbitrarily increased as in the 2D case. A study is performed for a network of tubes of an aspect ratio of 60 at a volume fraction of 10% for various values of C_{W,L_1}, C_{W,L_2}, and C_{W,L_3}. As the conductivity response surface will be a function of each of the cell width ratios, the response surface is studied for a fixed value of one of the cell width ratios and allowing the other two to vary. Figure 6.1 presents the conductivity surface for fixed values of $C_{W,L_1} = 5, 7, 9, 11, 13, 15$. Observe the gradient of the response surface approaches zero as $C_{W,L_2} \to 15$ and $C_{W,L_3} \to 15$. This can be observed in Figure 6.2 where the quivers represent the direction of the gradient of the conductivity surface where the length represents the magnitude of the gradient. It is interesting to note that as C_{W,L_2} is increased the predicted

conductivity decreases asymptotically, whereas for increasing C_{W,L_3} the conductivity increases asymptotically with neither independent variable showing a clear dominance over the other. In Figure 6.3 the response surface of conductivity is shown for fixed values of $C_{W,L_2} = 5, 7, 9, 11, 13, 15$. It is interesting to note that as $C_{W,L_3} \to 15$ the conductivity asymptotically increases, but there is no clear dependence on C_{W,L_1}. This is clearly seen in the quiver plot of Figure 6.4 where the gradient is almost exclusively aligned in the C_{W,L_3} direction, thus C_{W,L_3} is the dominating variable in relation to C_{W,L_1}. In Figure 6.5 the response surface of conductivity is shown for fixed values of $C_{W,L_3} = 5, 7, 9, 11, 13, 15$. It is interesting to note that as $C_{W,L_2} \to 15$ the conductivity asymptotically decreases, but as in Figure 6.3 where the response surface was for a fixed C_{W,L_2} there is no clear dependence on C_{W,L_1} as can be seen in the quiver plot of Figure 6.6 where the gradient is almost exclusively aligned along the C_{W,L_2} axis. Thus C_{W,L_2} is the dominating variable in relation to C_{W,L_1}. One can infer from Figure 6.1-Figure 6.5 that the dominating variables are the cell dimensions in the direction of current flow x_2 and, somewhat surprisingly, the thickness of the direction perpendicular to the plane in which the tubes are oriented. This observation has consequences when there are computational limitations for solving the network. For example, in the later studies using the nanotube lengths and diameters sampled from the Weibull distributions published in [1], a network for $C_{W,L_1} = C_{W,L_2} = C_{W,L_3} = 6$ had over $2,000,000$ contacts and $35,000$ tubes.

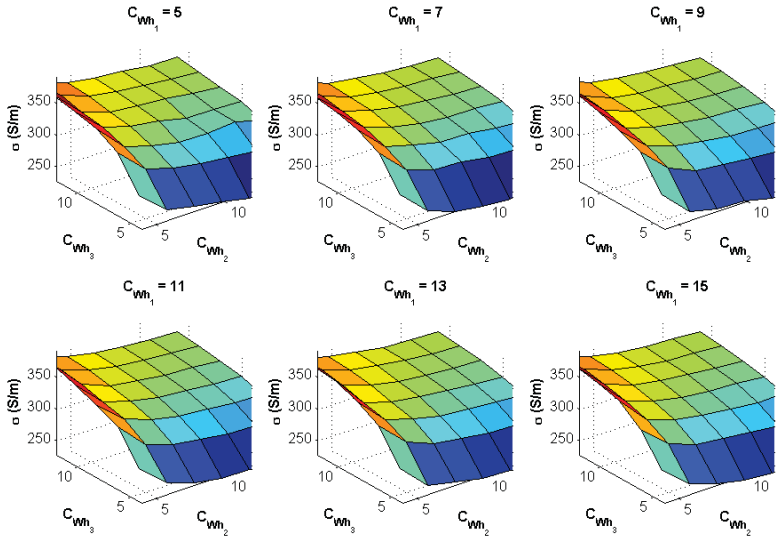

Figure 6.1: Response surface as a function of varying C_{W,h_2} and C_{W,h_3} predicted network conductivity for select cell width ratios in the x_1 direction, C_{W,h_1}.

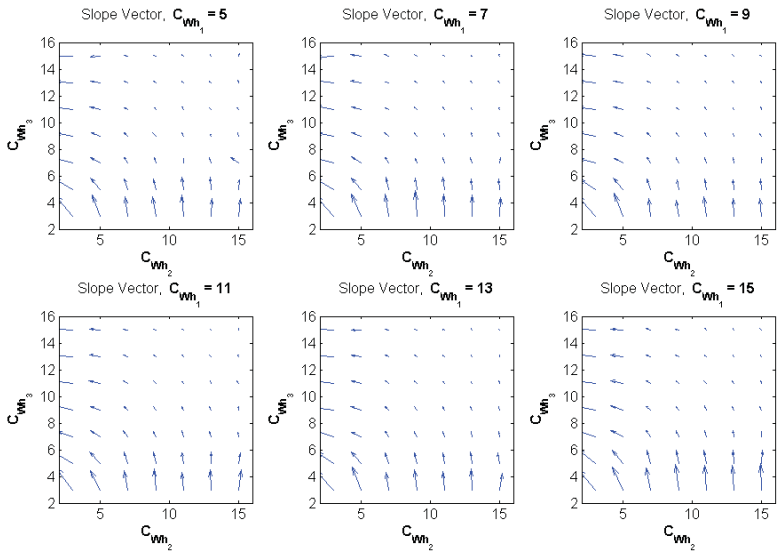

Figure 6.2: Quiver plot of response surface slope vector for predicted network conductivity for select cell width ratios in the x_1 direction, C_{W,h_1}.

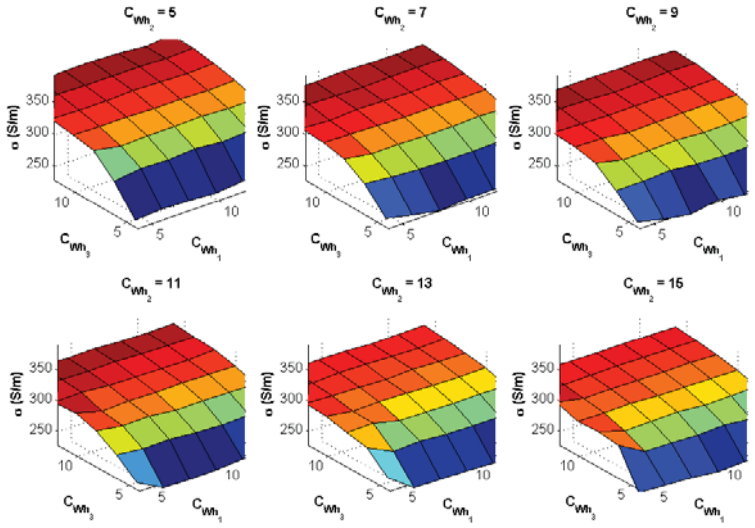

Figure 6.3: Response surface as a function of varying C_{W,h_1} and C_{W,h_3} predicted network conductivity for select cell width ratios in the x_2 direction, C_{W,h_2}.

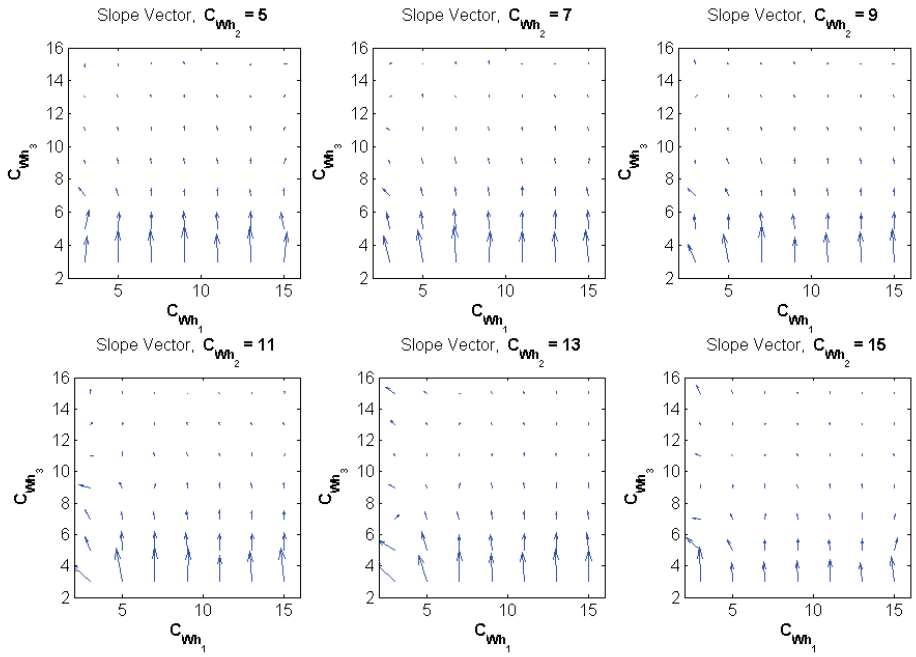

Figure 6.4: Quiver plot of response surface slope vector for predicted network conductivity for select cell width ratios in the x_2 direction, C_{W,h_2}.

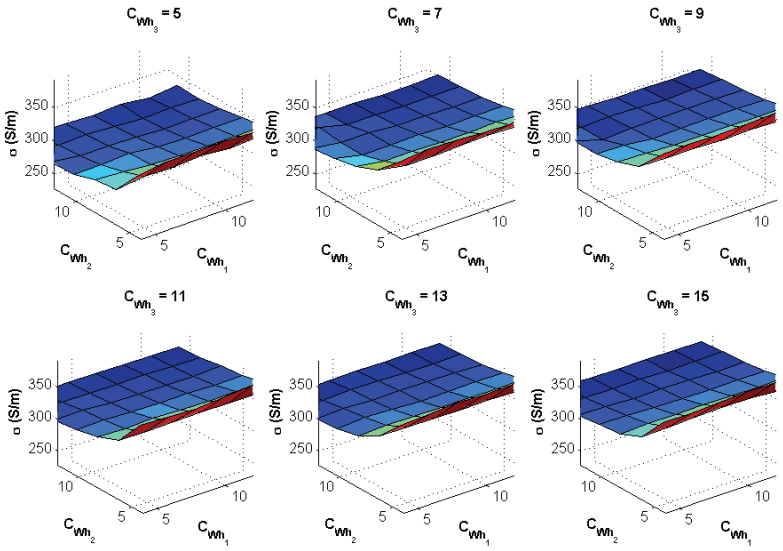

Figure 6.5: Response surface as a function of varying C_{W,h_1} and C_{W,h_2} predicted network conductivity for select cell width ratios in the x_3 direction, C_{W,h_3}.

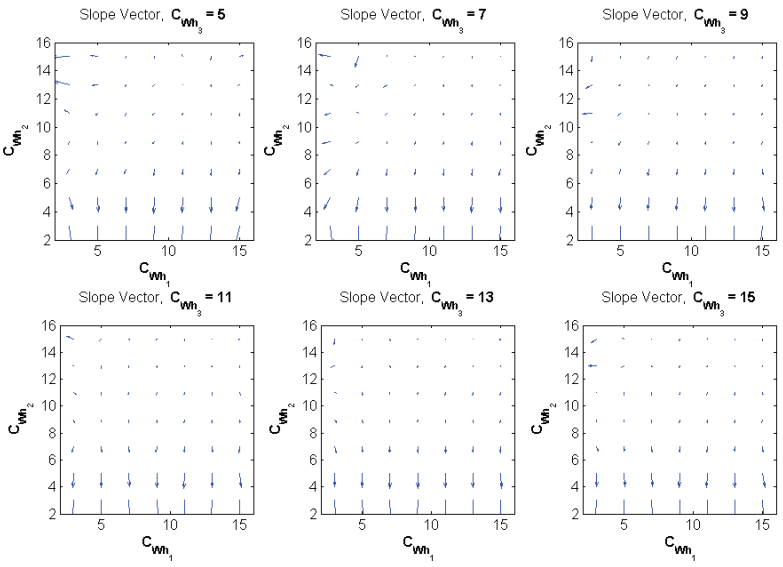

Figure 6.6: Quiver plot of response surface slope vector for predicted network conductivity for select cell width ratios in the x_3 direction, C_{W,h_3}.

6.2 Parametric Sensitivity Analysis

A numerical experiment is performed to quantify the effect of various stochastic inputs on the output response of the system. The goal of this case study is to determine the influence of each of the parameters and more importantly to determine those for which the output is most sensitive. There are several strategies to conduct this sensitivity analysis, and these will depend on the type of parameters and the experimental constraints. In order to extract appropriate and relevant information from any experiment, the scientific approach to planning the experiment should be employed. There are two common methods to quantify the relative importance of the design parameters within the experiment (a) Design of Experiment, and (b) Statistical analysis of the data obtained. These two methods each have their strong suits, but in the present scope the method of the full stochastic analysis is chosen due to its ability to handle the stochastic nature of the conductivity from our 3D network conductivity model. Here we present the approach we adapted to test the sensitivity of electrical and thermal conductivities from our model, on the input parameters.

6.2.1 Selection of Parameters

The conductivity behavior of a thin film network is influenced by several parameters of individual CNTs like length distribution, diameter distribution, chirality distribution, orientation distribution, etc. Yeh [1] from her experimental observations using SEM imaging reported that the length and the diameter follow a Weibull distribution given by the Equation (3.24). For a weibull distribution a change in the scale parameter α has the same effect on the distribution as the change of the abscissa scale. Increasing the value of α while holding β constant has the effect of stretching out the pdf. Since the area under a pdf curve is a constant value of one, the peak

of the pdf curve will also decrease with the increase of α. The Weibull shape parameter, β, is also known as the slope, as the value of β is equal to the slope of the regressed line in a probability plot. Different values of the shape parameter can have marked effects on the behavior of the distribution. It is of interest to determine the sensitivity of the bulk conductivity to the variables α and β, and what the error in the bulk conductivity will be due to experimental error from the input parameters. In other words, is there a chance that the inappropriate selection of the parameters α and β for the length and the diameter will drastically result in a significant alteration in the prediction of the conductivity. If yes, how drastic is the effect? Hence, the parameters α and β for the length and the diameter distributions will constitute the parameters for our study.

The sensitivity can be quantified as the product of the mean value of the design parameter multiplied by the gradient of the result variable (in this case the conductivity) in the direction of the design parameter. Due to the stochastic nature of the network conductivity, it is difficult to compute these partial derivatives for the gradient. To numerically approximate a derivative, a simple approach, such as a forward difference method, will increase in accuracy as the step size decreases. Mathematically,

$$\mu_P \frac{\partial \sigma}{\partial P} \approx \left(\frac{P_0 + P_1}{2} \right) \left(\frac{\sigma_0 - \sigma_1}{P_0 - P_1} \right) \tag{6.1}$$

where, μ_P is the average of the default value of the parameter and the changed parameter, $\partial\sigma$ represents the change in the conductivity (applies to both electrical and thermal conductivities. ∂P the change in the parameter, Subscripts 0 and 1 are the respective values for the default system and the system with the changed parameter.

6.2.2 Determination of Sample Size

In order to reasonably predict the conductivity, appropriate sample size should be determined. Statistically, larger sample size leads to increased precision in estimating properties regarding a population using Monte Carlo simulations. But due to computational and time constraint, we need to restrict our sample size big enough to fairly predict the property. In order to determine the appropriate sample size for this study we ran 341067 runs for our analytical solution of fixed diameter case for thermal conductivity Figure 5.7. From these data points we randomly selected 10 points and calculated its mean. We repeated this step for 2000 times and for each time we compared the mean with the total population mean to get the error. We then calculated the mean of these 2000 error values and tabulated it in Table 6.1. Similar procedure was adapted for the sample size of 100, 1000, $10,000$, $15,000$, $20,000$, $30,000$, $50,000$ and $100,000$. Figure 6.7 shows the plot of maximum error in calculating the mean for a sample size to the sample size. From the plot it can be seen that as the sample size increases, the accuracy in predicting the conductivity increases. We found the sample size of $20,000$ fairly large enough, to predict the conductivity behavior using this model. Hence, for all the studies our sample size will be $20,000$.

6.2.3 Determination of Appropriate Perturbation Size

Unfortunately, due to the uncertainty in the value of the function due to the stochastic nature of the simulations, it is required to increase the step size as large as possible, but as the error associated with approximating the partial derivative employing the forward difference method is directly related to the step size, hence, we need to keep it as small as possible. Thus there are two conflicting requirements. In order to get an idea of the appropriate step size, we perform our study for a

Table 6.1: Table of sample size and mean error.

Sample Size	Mean Error (W/m-K)
10	0.3068
100	0.0949
1000	0.0303
10000	0.0090
15000	0.0074
20000	0.0062
30000	0.0048
50000	0.0032
100000	0.0013

function where the solution is already known. Using the study depicted in Figure 5.9, where the diameter and chirality ratio is fixed and are both constants. The length is sampled from a constant function and samples are performed at various values of the length. Figure 5.9, shows the plot for increasing length and the resulting power law curve fit function (with $R^2 = 0.998$). To obtain the value of the gradient of the conductivity as a function of the change in length, we choose to run simulations with step sizes of 0.1%, 1% and 5% from the base length of 0.4μm. We ran $20,000$ runs for each simulation and present the histograms for each step size. Figure 6.8 shows the histograms for increasing bundle length. Histogram in red depicts the distribution of the electrical conductivity with the bundle length of 0.4μm. The mean conductivity for this bundle length is 1032900 S/m. In the same figure, the histogram in green represents the distribution of electrical conductivity for bundle length of 0.4004μm, which is 0.1% increase in the base length. The histogram in blue presents the distribution of electrical conductivity for bundle length of 0.404μm, which is 1% increase to the base length. The mean conductivity for this length is 1052700S/m. Finally, the histogram in black, shows the distribution of electrical conductivity for

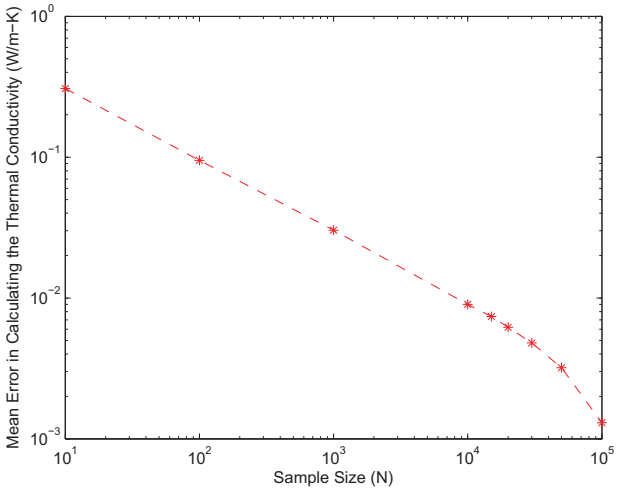

Figure 6.7: Decreasing error in approximating the population mean with increasing sample size.

Table 6.2: Sensitivity results for electrical conductivity for increasing length.

Length (μm)	%Change	$\mu_{L0}\frac{d\sigma}{dL}$ (Analytical)	$\mu_{L0}\frac{d\sigma}{dL}$ (M-C)
0.4	0	1.999×10^4	
0.4004	0.1		2.04×10^4
0.404	1.0		1.98×10^4
0.42	5.0		2.06×10^4

the bundle length of 0.42μm, a 5% increase in the base length. There is significant increase in the electrical conductivity as we notice the shift in the abscissa. The mean electrical conductivity for this length is 1133600S/m. Table 6.2, shows the comparison for the analytical values with the one obtained from the simulations. The analytical solution for electrical system was obtained from the Equation 5.12.

From Table 6.2, comparing the values in column(4), with column(3) we can see that, the Monte-Carlo simulation results for 1% increase produces result close to the one predicted analytically (i.e. column(3)). A smaller step size is preferred in order

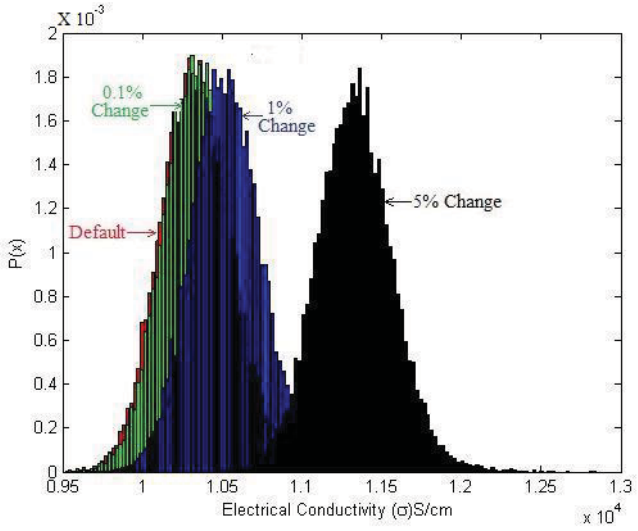

Figure 6.8: Histograms showing the frequency distribution of electrical conductivity for increasing bundle length.

to get better results from finite difference methods. Hence, we will select the step size of 1% for the bundle length for electrical conductivity sensitivity analysis. From Table 6.2, a comparison for the values of the change in conductivity per unit length obtained numerically using Monte-Carlo simulations (column 4) are contrasted with the change in conductivity per unit length obtained analytically (column 3). It is not surprising that the small step of 0.1% has the largest error due to the significant overlap of the obtained distributions for conductivity, and thus a small error in the conductivity expectation will result in a large error in the conductivity sensitivity. On the other hand, since the error in a forward difference method is on the order of the step size raised to the first power, it is anticipated that the error will increase with increasing step size. Thus, from our results it is not surprising that 1% provides a reasonable approximation of the derivative, and the future studies will rely on this step size.

Table 6.3: Sensitivity results for thermal conductivity for increasing length.

Length (μm)	%Change	$\mu_{L0}\frac{d\kappa}{dL}$ (Analytical)	$\mu_{L0}\frac{d\kappa}{dL}$ (M-C)
0.5	0	24.96	
0.5005	0.1		35.1
0.505	1.0		24.1
0.525	5.0		25.3

Similarly, Figure 5.7 shows the trends of changing thermal conductivity with increasing length. The base bundle length of 0.5μm was chosen for this study. We ran 20,000 runs for each simulation and chose the same step sizes of 0.1%, 1% and 5% from the base length. Figure 6.9 shows the histograms for changing thermal conductivity with increasing bundle length. Histogram in the red depicts the distribution of electrical conductivity with the bundle length of 0.5μm. The mean thermal conductivity for this bundle length was 13.22 W/mK. Histogram in green presents the histogram for bundle length of 0.5005μm, which is 0.1% increase in the base length. The mean thermal conductivity for this length is 13.26 W/mK. Similarly, the histogram in blue presents the thermal conductivity distribution for bundle length of 0.505μm, which is 1% increase to the base length. The mean conductivity for this length is 13.46W/mK. Histogram in black, presents the thermal conductivity distribution for bundle length of 0.525μm, a 5% increase in the base length. The mean thermal conductivity for this length is 14.45W/mK. Table 6.3, shows the comparison for analytical values with the one obtained from the simulations. The analytical solution for electrical system was obtained from the Equation 5.8

For the thermal system the results are tabulated in Table 6.3. It can seen from the column 3 and column 4, that both the step size of 1% provides result close

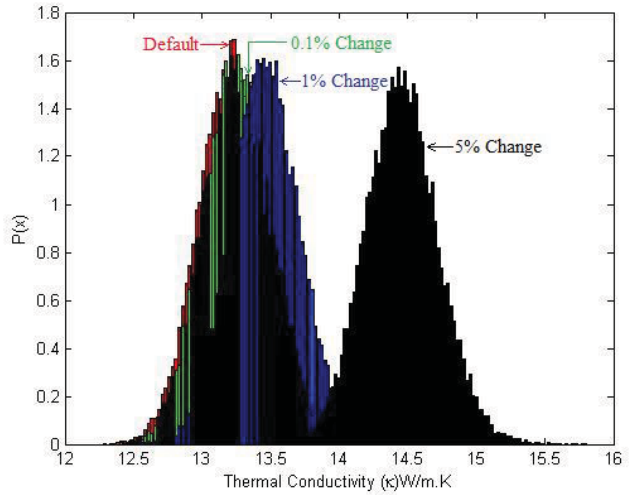

Figure 6.9: Histograms showing the frequency distribution of thermal conductivity for increasing bundle length.

to the analytical solution. Hence, for the thermal length parameter our step size will be 1%.

Next, we tested the diameter dependence on the electrical and thermal conductivity. As can be seen from Figure 5.12, the electrical conductivities decrease with increasing diameter. In order to test the sensitivity of the weibull parameters for diameter, similar procedure was adopted as discussed above for length. For a mixed network of carbon nanotubes, the electrical conductivity is related to the bundle diameter as given in Equation 5.16

Figure 5.14 shows the trends of changing thermal conductivity with increasing length. For this study, the bundle length is fixed to 20μm and the base bundle diameter was chosen to be 20nm. We ran 20, 000 runs for each simulation and chose the same step sizes of 0.1%, 1% and 5% from the base length. Figure 6.10 shows the histograms for decreasing electrical conductivity with the increasing bundle diameters. To begin with, the histogram in red depicts the distribution of electrical

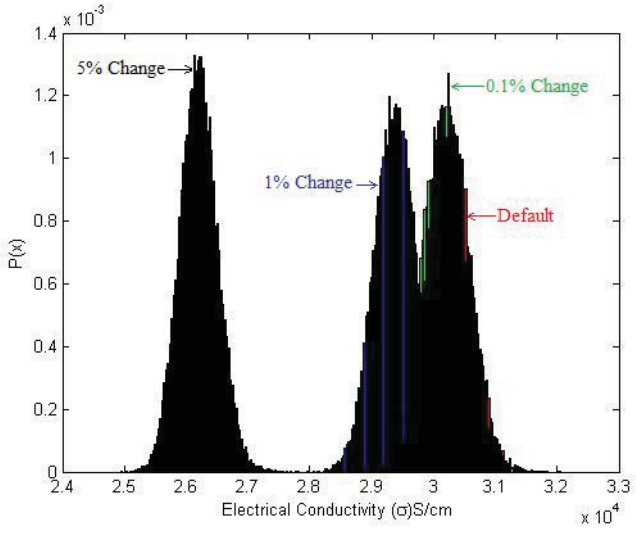

Figure 6.10: Histograms showing the frequency distribution of electrical conductivity for increasing bundle diameter.

conductivity for the bundle diameter of 20nm. The mean electrical conductivity for this bundle diameter is 3026000 S/m. Green histogram presents the distribution of electrical conductivity for bundle diameter of 20.02nm, which is 0.1% increase in the base diameter. The mean electrical conductivity for this diameter is 3017400 S/m. Histogram in blue depicts the distribution of electrical conductivity for bundle diameter of 20.20nm, which is 1% increase to the base diameter. The mean conductivity for this diameter is 2938300 S/m. Finally, the histogram in black, presents the distribution of electrical conductivity for bundle diameter of 21nm, a 5% increase in the base diameter. Table 6.4 tabulates the comparison for the values of the change in electrical conductivity per unit diameter obtained numerically using Monte-Carlo simulations (column 4) with the change in conductivity per unit diameter obtained analytically (column 3). It is clear from the table that 1% change gives a better approximation of the derivative, and the final study for electrical conductivity will be based on this step size.

Table 6.4: Sensitivity results for electrical conductivity for increasing diameter.

Diameter (nm)	%Change	$\mu_{d0}\frac{d\sigma}{dd}$ (Analytical)	$\mu_{d0}\frac{d\sigma}{dd}$ (M-C)
20.00	0	-8.922×10^4	
20.02	0.1		-8.59×10^4
20.20	1.0		-8.82×10^4
21.00	5.0		-8.32×10^4

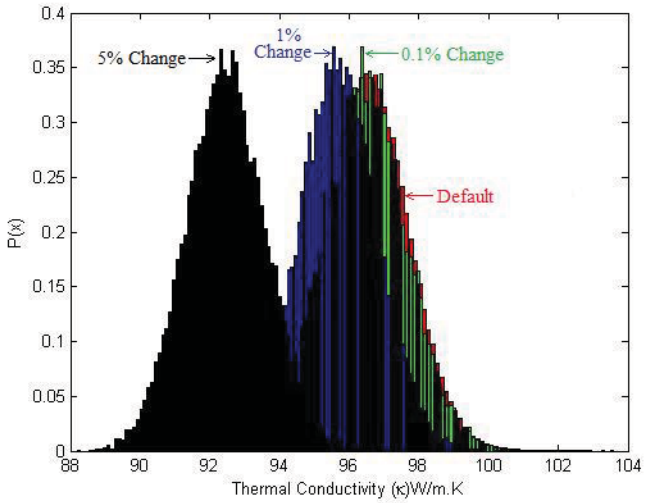

Figure 6.11: Histograms showing the frequency distribution of thermal conductivity for increasing bundle diameter.

A similar study on the diameter for the thermal conductivity is also performed. From Figure 5.14, we see that the thermal conductivity is related to the bundle diameter as given in the Equation 5.18. For this study, the bundle length is fixed to 20μm and the base bundle diameter is chosen to be 20nm. We ran 20,000 runs for each simulation and chose the same step sizes of 0.1%, 1% and 5% from the base diameter. Figure 6.11 shows the histograms for decreasing thermal conductivity with increasing diameter. The red histogram represents the distribution of electrical conductivity for bundle diameter of 20nm. The mean thermal conductivity for this

Table 6.5: Sensitivity results for thermal conductivity for increasing diameter.

Diameter (nm)	%Change	$\mu_{d0}\frac{d\kappa}{dd}$ (Analytical)	$\mu_{d0}\frac{d\kappa}{dd}$ (M-C)
20	0	-85.49	
20.02	0.1		-92.08
20.20	1.0		-85.23
21.00	5.0		-84.31

bundle diameter is 96.57 W/mK. The green histogram on the other hand presents the distribution of the thermal conductivity for the bundle diameter of 20.02nm, which is 0.1% increase in the base diameter. The mean thermal conductivity for this diameter is 96.47 W/mK. Similarly, the blue histogram presents the distribution of the thermal conductivity for the bundle diameter of 20.20nm, which is 1% increase to the base diameter. The mean conductivity for this diameter is 95.7 W/mK. Finally, the black histogram presents the distribution of the thermal conductivity histogram for the bundle diameter of 21nm, a 5% increase in the base diameter. The mean conductivity for this diameter is 92.45 W/mK. Table 6.5 tabulates the comparison for the values of the change in thermal conductivity per unit diameter obtained numerically using Monte-Carlo simulations (column 7) with the change in conductivity per unit diameter obtained analytically (column 6). It is clear from the table that 1% change gives a better approximation of the derivative, and the final study for thermal conductivity will be based on this step size.

6.2.4 Results

Based on the studies discussed in the previous section, we concluded that the step size of 1% was appropriate for all of our parameters. We then ran 5 different tests in order to determine the sensitivity of the model on the α and the β parameters of

Table 6.6: Relative sensitivity of the electrical conductivity to the weibull parameters.

Testing Parameter	Mean Conductivity	Final Sensitivity	Relative sensitivity
Default	174300		
Diameter (α)	175230	93500	0.28
Diameter (β)	172420	189000	0.57
Length (α)	177600	332000	1.00
Length (β)	172430	188000	0.57

Table 6.7: Relative sensitivity of the thermal conductivity to the weibull parameters.

Testing Parameter	Mean Conductivity	Final Sensitivity	Relative sensitivity
Default	226.02		
Diameter (α)	223.55	247.93	0.89
Diameter (β)	226.18	15.33	0.06
Length (α)	227.01	99.41	0.36
Length (β)	223.25	278.57	1.00

the length and the diameter. The results for the electrical conductivity are tabulated in Table 6.6. From the Table, it is clear that, amongst the parameters under study, electrical model is most sensitive to the α parameter of the weibull distribution for length. Another interesting, fact worth noting is that, increase in the α) parameter of length and diameter by 1% over predicts the electrical conductivity, whereas increase in the β parameter by the 1% under predicts it by the same amount for length and diameter.

Table 6.7, tabulates the sensitivity results for the thermal model. From the table, we can conclude that, the thermal conductivity is most sensitive to the β parameter of the length and to an extent, on the α parameter of the diameter.

This case study also demonstrates the effectiveness of the approach used. This approach is very general and can be used to test the sensitivity of the output attributed to any variation in the input parameters. The results obtained from the Monte Carlo simulations are in agreement with those obtained from the analytical solution for the simple system with an available analytic solution thus validating the approach, but the approach is more applicable for systems where the derivatives may not be evaluated analytically.

CHAPTER SEVEN

Conclusions, Limitations and Recommendations

This chapter discusses the conclusions drawn and certain shortcomings of the models. Accuracy of the model can be increased by incorporating additional information to the model. I have listed a few areas to look into it.

7.1 Conclusions

The objective of this project was to provide an insight into the thermal and electrical behavior of thin film carbon nanomembranes, a macro-scale network of neat single-walled carbon nanotubes (CNT), by developing computational simulations that stochastically incorporate the network nanostructure to understand the membrane's response to thermal and electrical loadings. In other words, we desired to establish a link between the stochastic nature of the nanostructure (like the bundle length, bundle diameter, chirality etc.) and the bulk response of the network. Originally, we started with a 2D model which provided us the feel for the complexity of the problem and the potential computational requirements. Soon we realized the flaw associated with what we termed our 2.5D assumption in Chapter Three. These inadequacies led to the need for a fully developed 3D model. In this work we present the required modification in the boundary conditions for the fully functional 3D model. The model depicted real 3D nanoscale thermal and electrical flow conditions, and the results were close to the experimental values reported in the literature with the consequence of drastically measured computational requirements.

With the validated model, several case studies were undertaken to quantify and comprehend the effect of stochastic nature of the nanostructure on the bulk

conductivity response. Determination of appropriate cell dimensions for the representative element is crucial. Hence, we started with the determination of the cell dimensions for the representative element. Based on the results from these simulations we selected to go with the cell width ratio of 10 for our 2D model, and 5 or 6 for our 3D model. We then started considering the input parameters for our study. From our case study on bundle length, we found that both the thermal and the electrical conductivity increases with the increasing bundle length. Also, a network consisting entirely of metallic tubes proved to have a better electrical conductivity as compared to a mixed network consisting of metallic and semiconducting tubes in ratio of $1:3$ but the improvement was only by a factor of $1.8 \sim 2$. The next study was performed on the diameter and unlike to the bundle length, both the electrical and the thermal conductivities decreased with the increasing bundle diameter. The network consisting entirely of metallic tubes proved to be a better option and the improvement in this case was on the order of a factor of 2. The present model can be used only for conditions above percolation, which occurs at very low volume fractions. The model was used to study the variation in the electrical conductivity for various volume fractions ranging from 0.5% to 70%. Apart from the factors mentioned, the conductivities also depend upon the orientation of tubes in a network. Interestingly, thermal and electrical conductivities show different trends for increasing orientation along the direction of the flow. This anomaly is also addressed in Chapter 5.

Apart from the case studies mentioned above we also present, a sensitivity analysis of the various nanostructure parameters using our 3D models. The first case study deals with the determination of the sensitivity of the dimensions of the representative elements. From the simulations it is clear that the dominating variables

are the cell dimensions along the direction of the flow and the cell dimensions perpendicular to the direction in which the tubes are aligned. But these parameters are due to the method used to construct the model. As long as the cell dimensions are sufficiently large this will not affect the model predictions. In another study we employed the models to investigate the sensitivity of the thermal and the electrical conductivity on the select stochastic parameters. In particular, we investigated the sensitivity of the network to errors in knowing the experimentally obtained Weibull probability distribution for length and diameter. The sensitivity results indicate that for the electrical conductivity response, the network is most sensitive to the length's Weibull distribution scale parameter. Conversely, for the thermal response it is actually the shape parameter of the length that causes the most significant change in the network conductivity.

7.2 Limitations of the Model

The models take in stochastic inputs such as the length, diameter, orientation distribution, chirality and as such will be limited in the predicted accuracy based on the confidence one has in these inputs. The models still can be used as a design tool, for a design engineer or a manufacturing engineer as it can provide trends thus helping them to focus their efforts on the parameters that will have the greatest impact on the final part performance. The models are sensitive to the intercontact distribution means,and the type of input probability distributions, hence a better understanding of this will greatly enhance the confidence in the accuracy of the model's results.

Another issue to be addressed is that of the computational limitation. As it presently stands, for the aspect ratio of tubes of 184 (this number comes from a related experimental studies) used frequently in this study, the cell width ratio was limited to 5 or 6 for the full 3D model. It was shown that this ratio needed to be at

least 10 for the tube of aspect ratio 30, to obtain an answer within 5% of an infinite cell. It is unclear how much the error is for the presented results, but this issue must be addressed in future studies.

The model only takes into account the intercontact resistance for the conductivity calculations and assumes the tubes to be resistanceless. In the physical system there should be some potential drop along the tube, and it has never been addressed how much this assumption may affect the final model results. Moreover, the tubes are also assumed to be defect free, but [24] showed that defects and vacancies does decrease the thermal conductivity along the nanotube. As the probability of a defect occurring at the point of contact is very low, hence this effect was not taken into account, but in future it may be worthwhile to study this issue and include it along with the tubes intrinsic resistance.

7.3 Scope for Future Work

There are some areas that may be studied in order to improve the accuracy of the predicted results. In this section we list a few of them. To begin with, we recognize that the contact resistance between the two tubes is a function of each tube's chirality and their relative rotation. There are two relevant rotations that can be considered; the rotation about the longitudinal axis (a parameter indirectly incorporated in our model), and the transverse axis rotation (the angle defined as θ in our model). For our thermal system, we have incorporated the results for the same from our MD simulation study. The study was done using a semiconducting $(5, 5)$ and a metallic $(5, 0)$ CNT. Unfortunately, these results are for just one set of carbon nanotubes and there is no rule of thumb that could be used to make these results general. The electrical model does not incorporate any of these results. As such, it

is constrained to assume that all the contacts are sampled from a uniform random distribution of contact resistances.

The second limitation is attributed to the out of plane angular rotation for each tube within the CNT networks, thus limiting the reasonableness of our parallel circuit assumption. Future work is suggested to form reasonable out-of-plane orientations and the resulting 3D symmetry conditions, thus forming a fully three-dimensional representative volume element. This will add to the computational complexity and contribute significantly to the solution resource requirements as the number of point of contacts would increase with the out of plane orientation.

The third area of suggested improvement is to account for the intrinsic resistance of each SWNT. It is anticipated that, there may be some potential drop along the tubes. The present model neglects intrinsic resistance by an order of magnitude argument, but this argument may be too constraining and may play a significant role in the physical characteristics of the CNT network.

Another area to look into would be chirality and temperature dependence of thermal and electrical conductivity. Suggested approach would be first dividing the nanotubes as armchair, zigzag and chiral based on their configuration (n, m), where n and m are the chiral vectors. The next step would be studying the thermal and electrical transport based of this (n, m) configuration. This would require a through understanding of thermal and electronic transport as well as molecular dynamics simulation techniques. Also, eventually it will require investments in Software package(s) like Accelrys Materials Studio(Discover module). Temperature dependence of the thermal and the electrical conductivity should also be incorporated based of the above studies and references like [17, 27, 28].

There may be other areas worth looking into for improvement. Using the sine/cosine 3D distribution is not physically possible for rod-like orientation distributions as there is a possibility of occupance of zero which is meaningless and hence the 3D distribution should be modeled by a physically meaningful orientation distribution, such as the Bingham distribution. Multi-walled nanotubes, may be worth studying as they are a cheaper alternative to SWNTs and will help to reduce the cost of component being manufactured or designed.

The model currently ignores the heat transfer between the thin film network and surrounding media, assuming the media to be air. It would be more meaningful if the interaction with the substrate/matrix surrounding the network were also considered while simulating the bulk conductivity. This may require understanding the mechanism of electron and phonon interaction with the substrate. This might me accomplished by dividing the overall resistivity of the system into three parts (1) Resistivity along the tube, (2) Resistivity between the tubes and surrounding matrix/resin and (3) Resistivity of the matrix/resin itself. Use of appropriate MD simulation software package is highly recommended to accomplish this task.

All the improvements suggested above would be demanding, especially in terms of computational requirements, it is highly desirirable to develop a parallelized version of the computations to solve Equation (4.21) as is is found that about 87% of the time is spent for solving it.

Finally, I would like to conclude with a vision that, in future, given a set of operating conditions for a component, the software suite would be able to optimize the cost of production, by giving out information regarding the fiber/bundle length, fiber/bundle diameter, chirality ratio, orientation and volume fraction of CNTs. These are the parameters that alter the thermal and electrical behavior of the

thin films. For instance, as we showed using case studies that pure metallic nanotubes are better when it comes to improving the electrical conductivity, but manufacturing pure metallic tubes incurs additional cost. Hence, knowledge of appropriate chirality ratio for a network is helpful. Also, as both the thermal conductivity as well as electrical conductivity vary with the length and the diameter of the individual nanotube hence, knowing appropriate dimensions of the nanotube would also help. The software suite would also be able to predict the performance of the component under the given set of conditions and lifespan. The next generations of this model will not be restricted to just CNTs and could be used for any fibers on any scale.

APPENDIX

VITA

Since his childhood, Nikhil closely observed and followed several industries in his local community - their growth, their downfall be it service related (like seaport and airport) or manufacturing (like the steel plant and chemical fertilizer plant). He was always fascinated with machines and their applications. He recognized that no matter which industry you take or whichever machine you use, there is abundant supply of engineering that must be put into application. This aroused his curiosity as well as planted the seed of passion towards engineering and shaped his choice of profession (as an engineer) at an early age.

He elected to pursue his engineering dreams at 'Shri Ramdeobaba Kamla Nehru Engineering College' (R.T.M. Nagpur University) and successfully completed the requirements of the Bachelor of Industrial Engineering program providing him with the tools to understand the human aspect of engineering problems.

He has worked as an intern at Grasim Industries Ltd., where he was underwent training in various aspects of machine, both technical (machining, maintenance etc) and non technical (Cost analysis, FMEA analysis etc). During the training period his performance was rated as Excellent.

His experience as an intern at Mahindra and Mahindra strengthened his belief that basic industrial engineering concepts can bring tremendous benefit to companies and personnel alike. His project was installed successfully in the facility and his endeavor was applauded. The project also received a star ranking, and was selected as an entry for company's regional awards.

In his final semester he worked on a project within the supply chain organization of India's largest English newspaper daily - The Times of India. With his engineering knowledge and experience obtained from the previous two employers, he identified areas for improvement and also recommended methods to manage the supply chain of the newspaper daily more effectively in their current circulation as well as scenarios forecast five years into the future.

He joined Florida State University, as a graduate student in Industrial and Manufacturing Engineering, in the fall semester of 2007. At FSU He got the opportunity to work with Dr. David Jack, as his graduate Research Assistant. There after he moved to Baylor University in the fall of 2009, with Dr. David Jack to continue his graduate degree in Mechanical Engineering. He has showcased his research at various international technical conferences like ASME-IMECE (2009, 2010 and 2011) and ASME-ECTC (2010, 2011). He also has his research papers under review within ASME journals. He also peer reviewed four conference papers for ASME-IMECE-2010

His short term goals include gaining experience as a manufacturing engineer and use his knowledge to improve manufacturing processes and designs. In long term he plans to setup a manufacturing unit and help develop the villages in India, by providing employment and education in the rural areas.

BIBLIOGRAPHY

[1] C. S. Yeh. A study of nanostructure and properties of mixed nanotube buckypaper materials: fabrication, process modeling characterization and property modeling. *Ph.D. thesis, Florida State University*, 2007.

[2] S. Iijima. Helical microtubules of graphitic carbon. *Nature*, **354**:56–58, 1991.

[3] Rodney S. Ruoff, D. Qian, and W.K. Liu. Mechanical properties of carbon nanotubes: theoretical predictions and experimental measurements. *C. R. Physique*, 4:993–1008, 2003.

[4] J. Tersoff and R.S. Ruoff. Structural properties of a carbon-nanotube crystal. *C. R. Physique*, **73**:676–679, 1994.

[5] Y.K. Kwon and D. Tomanek. Electronic and structural properties of multiwall carbon nanotubes. *PHYSICAL REVIEW B*, **58**, 1998.

[6] L. Langer, V. Bayot, E. Grivei, J. Issi, C. Olk, L. Stockman, C. Haesendonck, and Y. Bruynseraede. Quantum transport in a multiwalled carbon nanotube. *Physical review letters*, **76**(3):479–482, 1996.

[7] L. Chico, V. H. Crespi, L. X. Benedict, S. G. Louie, and M. L. Cohen. Thermal conductance and thermopower of an individual single-wall carbon nanotube. *Physical Review Letters*, 76(6):971974, 1996.

[8] D.A. Jack, Z. Liang, S. Li, C. Yeh, and J. Fielding. Statistical planar conductivity model of orientationally dependant carbon nanotube network buckypapers. In *SAMPE'09*, Baltimore, MD, May 2009. SAMPE.

[9] S. Kumar, N. Pimparkar, J.Y. Murthy, and M.A. Alam. Theory of transfer characteristics of nanotube network transistors. *Applied Physics Letters*, **88**(12), 2006.

[10] T. Pichler, M. Knupfer, M.S. Golden, J. Fink, A. Rinzler, and R.E. Smalley. Localized and delocalized electronic states in single-wall carbon nanotubes. *Physical Review Letters*, **80**(21):4729–4732, 1998.

[11] A. Nieuwoudt and Y. Massoud. On the impact of process variations for carbon nanotube bundles for vlsi interconnect. *IEEE Transactions on Electron Devices*, **54**(3):446–455, 2007.

[12] N. Pimparkar and M. A. Alam. A bottom-up redefinition for mobility and the effect of poor tubetube contact on the performance of cnt nanonet thin-film transistors. *IEEE Electron Device Letters*, **29**(9):1037–1039, 2008.

[13] S. Kumar, M.A. Alam, and J.Y. Murthy. Computational model for transport in nanotube-based composites with applications to flexible electronics. *Journal of Heat Transfer*, **129**:500–508, April 2007.

[14] S. Hasan, M. A. Alam, and M. S. Lundstrom. Simulation of carbon nanotube fets including hot-phonon and self-heating effects. *IEEE Transactions on Electron Devices*, **54**(9):2352–2361, 2007.

[15] C. Yu, L. Shi, Z. Yao, D. Li, and A. Majumdar. Thermal conductance and thermopower of an individual single-wall carbon nanotube. *Nano Letters*, **5**(9):1842–1846, 2005.

[16] H. Zhong and J. R. Lukes. Interfacial thermal resistance between carbon nanotubes: Molecular dynamics simulations and analytical thermal modeling. *Physical Review B*, 74:125403–(1–10), 2006.

[17] M. Osman and D. Srivastava. Temperature dependence of the thermal conductivity of single-wall carbon nanotubes. *Nanotechnology*, **12**:21–24, 2001.

[18] D. Yang, Q. Zhang, G. Chen, S. Yoon, J. Ahn, and J. Li. Thermal conductivity of multiwalled carbon nanotubes. *PHYSICAL REVIEW B*, **66**:165440–(1–6), 2002.

[19] Venkateswara, U, D., and Rao, A, M., and Eklund P, C. Probing the single-wall carbon nanotube bundle: Raman scattering under high pressure. *PHYSICAL REVIEW B*, **59**, April 1999.

[20] L. Zheng, M. O'Connell, S. Doorn, X. Liao, Y. Zhao, E. Akhadov, E. Hoffbauer, B. Roop, Q. Jia, R. Dye, D. Peterson, S. Huang, J. Liu, and Y. Zhu. Ultralong single-wall carbon nanotubes. *Nat Mater*, **3**(10):673–676, oct 2004.

[21] Hone J., M. Llaguno, N. Nemes, and A. Johnson. Electrical and thermal transport properties of magnetically aligned single wall carbon nanotube films. *Applied Physics Letters*, **77**(5):666–668, 2006.

[22] P. Gonnet, Z. Liang, E. Choi, R. Kadambala, C. Zhang, J. Brooks, B. Wang, and Kramer L. Thermal conductivity of magnetically aligned carbon nanotube buckypapers and nanocomposites. *Current Applied Physics*, **6**:119–122, 2006.

[23] H. Ming, S. Shenogin, P. Keblinski, and N. Raravikar. Thermal energy exchange between carbon nanotube and air. *Applied Physics Letters*, **90**(23), 2007.

[24] J. Che, T. Cagin, and W. Goddard III. Thermal conductivity of carbon nanotubes. *Nanotechnology*, **11**:65–69, 2000.

[25] Zhang, W., Zhiyuan Zhu, Feng Wang, Tingtai Wang, Litao Sun, and Zhenxia Wang. Chirality dependence of the thermal conductivity of carbon nanotubes. *Nanotechnology*, **15**:936–939, 2004.

[26] K. Bi, Y. Chen, J. Yang, Y. Wang, and M. Chen. Molecular dynamics simulation of thermal conductivity of single-wall carbon nanotubes. *Physics letters A*, **350**:150–153, 2006.

[27] J. Hone, M. Llaguno, N. Nemes, and A. Johnson. Thermal conductivity of single-walled carbon nanotubes. *Applied Physics Letters*, **77**(5):666–668, 1999.

[28] P. Kim, L. Shi, A. Majumdar, and P. McEuen. Mesoscopic thermal transport and energy dissipation in carbon nanotubes. *Physica B: Physics of Condensed Matter*, **323**:67–70, 2002.

[29] Motoo, F., and Zhang, X. and Xie, H. and Ago, H. and Takahshi, K. and Ikuta, T. and Abe, H. and Shimizu, T. Measuring the thermal conductivity of a single carbon nanotube. *Physics Review Letters*, **95**, 2005.

[30] S. Wang, Z. Liang, C. Zhang, and B. Wang. Dispersion and thermal conductivity of carbon nanotube composites. *Carbon*, **47**:53–57, 2009.

[31] A.V. Salvin, H. Bambi, and S. Kivshar. Thermal conductivity of single-walled carbon nanotubes. *PHYSICAL REVIEW B*, **80**, 2009.

[32] J. Tersoff. Contact resistance of carbon nanotubes. *Applied Physics Letters*, **74**:2122–2124, 1999.

[33] D. Hecht, H. Liangbing, and G. Gruner. Conductivity scaling with bundle length and diameter in single walled carbon nanotube networks. *Applied Physics Letters*, **89**(13):133112–(1–3), 2006.

[34] R. Haggenmuelle, J. Lukes, R. Fischer, John E. Winey, and I. Karen. Single wall carbon nanotube/polyethylene nanocomposites: thermal and electrical conductivity. *Macromolecules*, **40**:2417–2421, 2007.

[35] T. Pham, B. Park, S. Wang, Z. Liang, C. Zhang, B. Wang, P. Funchess, and L. Kramer. Mechanical and electrical properties of polycarbonate nanotube buckypaper composite sheets. *Nanotechnology*, **19**, 2008.

[36] J. Park, S. Li, R. Liang, X. Fan, C. Zhang, and B. Wang. The high current-carrying capacity of various carbon nanotube-based buckypapers. *Nanotechnology*, **19**, 2008.

[37] Y. Tian, Q. Cheng, J. Park, Z. Liang, C. Zhang, and B. Wang. The fabrication of single-walled carbon nanotube/polyelectrolyte multilayer composites by layer-by-layer assembly and magnetic field assisted alignment. *Nanotechnology*, **20**:3219–3225, 2009.

[38] Q. Cheng, J. Bao, J. Park, Z. Liang, C. Zhang, and B. Wang. High mechanical performance composite conductor: multi-walled carbon nanotube sheet/bismaleimide nanocomposites. *Advanced Functional Materials*, **19**:3219–3225, 2009.

[39] J. Park, J. Smithyman, Z. Liang, C. Zhang, B. Wang, P. Funchess, and L. Kramer. Electromagnetic interference shielding properties of carbon nanotube buckypaper composites. *Nanotechnology*, **20**, 2009.

[40] J. Park, N. Yun, Z. Liang, C. Zhang, and B. Wang. Single-walled carbon nanotube buckypaper and mesophase pitch carbon/carbon composites. *Carbon*, **48**, 2010.

[41] D. Jack. Modeling and simulation of swnt buckypaper electrical conductivity. *AFRL Report*, 2010.

[42] R. Hogg, J. McKean, and A. Craig. Introduction to mathematical statics. *Pearson/Prentice Hall Press, New Jersey*, 2005.

[43] N. Ashtekar and D.A. Jack. Stochastic modeling of the bulk thermal conductivity for dense carbon nanotube networks. In *Proceedings of the IMECE'09*, Orlando, FL, November 2009. ASME.

[44] D.A. Jack, C. S. Yeh, Z. Liang, S. Li, J.G. Park, and J.C. Fielding. Modeling and experimental study of dense packed carbon swnt network electrical conductivity. *Nanotechnology*, **21**, 2010.

[45] J. N. Reddy. An introduction to the finite element method. *McGraw Hill Press, Massachusetts*, 2006.

[46] R. Satio, G. Dresselhaus, and M.S Dresselhaus. Physical properties of carbon-nanotubes. *Imperial College Press, London*, 1998.

[47] N. Ashtekar and D.A. Jack. Parametric study of thermal and electrical behaviour of 3d cnt thin film networks. In *Proceedings of the IMECE'10*, Vancouver, British Columbia, Canada, November 2010. ASME.

[48] N. Ashtekar and D.A. Jack. Computational investigation of thermal and electrical parameter sensitivity of neat cnt thin film networks. In *Proceedings of the SPDC-ECTC*. ASME, March 2011.

[49] P.R. Bevington and K. Robinson. Data reduction and error analysis for the physical sciences. *WCB/McGraw-Hill*, 1992.

[50] N. Ashtekar and D.A. Jack. Computational parametric investigation of thermal conductivity of a 2d neat cnt thin film network. In *Proceedings of the SPDC-ECTC*, Tulsa, OK, March 2010. ASME.